2008

Pattern Recognition of a Gravitational Wave Pulsar Signal

Marc Eric Normandin
Western University

Recommended Citation

Normandin, Marc Eric, "Pattern Recognition of a Gravitational Wave Pulsar Signal" (2008). *Digitized Theses*. 4818.
https://ir.lib.uwo.ca/digitizedtheses/4818

Pattern Recognition of a Gravitational Wave Pulsar Signal

(Spine title: Pattern Recognition of a Gravitational Wave Pulsar Signal)

(Thesis format: Integrated)

by

Marc Eric Normandin

Graduate Program
in
Physics and Astronomy

A thesis submitted in partial fulfillment
of the requirements for the degree of
Master of Science

School of Graduate and Postdoctoral Studies
The University of Western Ontario
London, Ontario, Canada

Certificate of Examination

THE UNIVERSITY OF WESTERN ONTARIO
SCHOOL OF GRADUATE AND POSTDOCTORAL STUDIES
CERTIFICATE OF EXAMINATION

Chief Adviser:

Dr. Sreeram Valluri

Advisory Committee:

Dr. Shantanu Basu

Dr. David F. Gray

Examining Board:

Dr. Shantanu Basu

Dr. Lalu Mansinha

Dr. Paul Wiegert

The thesis by
Marc Eric Normandin
entitled:
Pattern Recognition of a Gravitational Wave Pulsar Signal
is accepted in partial fulfillment of the
requirements for the degree of
Master of Science

Date: ____________________

Chair of Examining Board
Firstname Lastname

Abstract

The *direct* detection of Gravitational Waves (GWs) is one of the most challenging problems in experimental gravitation today. It warrants the use of highly advanced large laser interferometers such as LIGO, VIRGO, LISA, TAMA 300, GEO 600 and AIGO. The analysis of the data from such instruments requires and combines the expertise from a multitude of scientific disciplines. The verification of a detected signal demands an effective way to distinguish the source signal from the background noise. Such a study is required for an all-sky search to determine the ϕ and θ angles on the sky of gravitational wave sources and their frequencies. In this thesis is presented analytical solutions and associated numerical approximations for the inner products employed in matched filtering using templates, a form of pattern recognition, applied to a GW pulsar signal. An exact closed-form expression for the inner products is rigourously derived using the special functions of mathematical physics. The inner products involve reciprocal Eulerian gamma functions, which occur in the study of many diverse phenomena. The spectral noise density of the VIRGO GW detector is shown to be amenable to analysis. Spectral noise densities like those for LIGO and GEO 600, although different and in a slightly more restricted frequency band, are likewise amenable. Numerical computation of the inner products, estimates of the computational time of the solution on serial and parallel computers, and the efficiency of the resulting algorithms are studied. The fitting factor that indicates the goodness of fit between a signal and a template is given in closed-form and computed numerically. The numerical plots display an approximate symmetry in the template ϕ and θ domain. Threshold crossing statistics are found, and the probability that a template is within a given radius of the signal is studied.

To my mother and father,
my love is with you forever.

Acknowledgements

During the course of this thesis research I encountered areas of physics, such as General Relativity, and areas of mathematics, such as the special functions of mathematical physics, which I was not very familiar with. Attending the course on mathematical methods taught by my wonderful supervisor Dr. Sree Ram Valluri was both enjoyable in and of itself, as well as quite beneficial for my research. Through both his vast knowledge, which he was always willing to share, and his continued guidance over more than a two year period, which was invaluable, my research steadily progressed and has resulted in this thesis. I am forever grateful to him for all that he has taught me in the realms of science and humanity. He is both a mentor and a friend, and I am truly fortunate to know him.

The numerical portion of my research would not have been possible without the use of excellent computer hardware. I thank SHARCNET (Shared Hierarchical Academic Research Cluster Network) for allowing me the use of the computational resources needed to obtain the numerical results appearing in this thesis.

I also extend my thanks to Manuel Gil for helping to greatly improve the writing of this manuscript, and to Dr. Tania Regimbau for providing information on the VIRGO spectral noise density.

My special thanks go to the anonymous reviewers of my 2007 Symbolic Numeric Computation [1] and 2008 Theoretical Computer Science [2] papers for their inspiring and thorough critiques that have raised many interesting questions concerning matched filtering, as well as stimulated interesting work.

Table of Contents

Certificate of Examination . . . . **ii**

Abstract . . . . **iii**

Dedication . . . . **iv**

Acknowledgements . . . . **v**

Table of Contents . . . . **vi**

List of tables . . . . **ix**

List of figures . . . . **x**

1 Introduction **1**
- 1.1 Overview 4
- 1.2 Thesis objectives 4
- 1.3 Thesis outline 4

2 Mathematical Review **6**
- 2.1 Pulsars 6
- 2.2 Differential geometry review 7
  - 2.2.1 The Einstein summation convention 9
- 2.3 General Relativity 11
  - 2.3.1 The spacetime metric 11
  - 2.3.2 The geodesic equation 12
- 2.4 Gravitational waves 12
  - 2.4.1 Linearized plane waves 13
  - 2.4.2 The effect of a gravitational wave 15
  - 2.4.3 Detector equation 17
- 2.5 GW signal waveform for a pulsar 18

3 Gravitational Wave Data Analysis **20**
- 3.1 Detection and measurement 20
- 3.2 Data analysis methods 22

4 Matched Filtering using Templates 25
4.1 Maximum likelihood estimation 25
4.2 Matched filtering using templates 27
4.2.1 The inner product 28
4.2.2 The fitting factor 29
4.3 The spectral noise density 30
4.4 The lattice covering 33
4.5 Summary of the analysis method 38

5 The Model GW Signal 40
5.1 The Fourier transform of the model signal 41
5.2 Reexpression of $H_+(B_f)$ 44
5.2.1 The exponentials 44
5.2.2 The generalized hypergeometric function 45
5.2.3 The final form of $H_+(B_f)$ 45

6 Derivation of the Inner Product 47
6.0.4 Integral solution when $j \neq \bar{j}$ 49
6.0.5 Integral solution when $j = \bar{j}$ 50
6.0.6 Inner product expression snapshot 51
6.0.7 Elimination of the summation over j 51
6.0.8 Final form of the inner product solution 52
6.1 Bounds for the summands 53

7 Numerical Implementation 56
7.1 Computer hardware 56
7.2 Computer libraries used 57
7.3 Problems and solutions 57
7.3.1 Truncation of the infinite series 59
7.3.2 Loss of precision 60
7.3.3 Underflows and overflows 61
7.3.4 Re-computation of time-costly summands 63
7.3.5 Summary of solutions 65

8 Numerical Studies **67**
8.1 Effects of the truncated indices 67
8.1.1 Inner product runtimes 69
8.1.2 Inner product values and errors 70
8.2 Pulsar parameter space studies 71
8.2.1 Full parameter plot 72
8.2.2 Azimuthal plot for $\theta_T = \theta_S$ 74
8.2.3 Azimuthal plot for $\theta_T = \theta_S + 90$ degrees 75
8.2.4 Colatitude plot for $\phi_T = \phi_S$ 76
8.2.5 Colatitude plot for $\phi_T = \phi_S + 180$ degrees 76
8.3 Frequency study 77
8.4 Threshold crossings 78
8.4.1 Threshold crossings for a single mesh 81
8.4.2 Total number of threshold crossings for 29 meshes 81
8.4.3 Probability of matching 83

9 Conclusions **90**
9.1 Achievements 92
9.2 Future Work 93

References **94**

Curriculum Vita **99**

List of Tables

4.1 Regular lattice template sizes 39

8.1 Inner product uniform index statistics 68

List of Figures

2.1 Pulsar schematic 7
2.2 Gravitational wave polarizations 15
2.3 Michelson interferometer 17

3.1 StackSlide analysis method 23

4.1 LIGO S4 strain 34
4.2 Matched filtering lattice algorithm 36
4.3 Adaptive search example 38

7.1 SHARCNET network map 58

8.1 Inner product runtimes. 69
8.2 Theoretical performance times. 71
8.3 Inner product values. 72
8.4 FF vs (ϕ_T, θ_T) 73
8.5 FF vs ϕ_T for $\theta_T = \theta_S$ 74
8.6 FF vs ϕ_T for $\theta_T = \theta_S + 90$ 75
8.7 FF vs θ_T for $\phi_T = \phi_S + 90$ 76
8.8 FF vs θ_T for $\phi_T = \phi_S + 180$ 77
8.9 Variation of template frequency. $\Delta f = 1$ Hz 78
8.10 Variation of template frequency. $\Delta f = 0.01$ Hz 79
8.11 Variation of template frequency. $\Delta f = 0.001$ Hz 80
8.12 Threshold crossings 81
8.13 Threshold crossings zoomed 82
8.14 Total number of threshold crossings 82
8.15 Threshold statistics 83
8.16 Parameter mesh #1 84
8.17 Parameter mesh #2 85
8.18 Parameter mesh #3 86
8.19 Parameter mesh #4 87
8.20 Parameter mesh #5 88
8.21 Parameter mesh #6 89

Chapter 1

Introduction

Gravity is geometry. That is the brilliant idea that Einstein gave to the world. A consequence of gravity being geometry is that a new type of radiation should exist. The radiation is called *gravitational radiation* or *gravitational waves.* A gravitational wave is described by a wave equation, and so shares the common properties of all waves such as having a wavelength, speed of propagation, and frequency. However, a great difference is in what is "waving." For water waves, what is waving is the water, for sound it is the pressure waves in air, and for electromagnetic waves it is fluctuating electric and magnetic fields. But for gravitational waves it is space and time itself that are theorized to be waving. To understand the gravitational waves requires a knowledge of Einstein's theory of General Relativity, which is expressed using differential geometry.

The detection of gravitational waves (GWs) is one of the greatest challenges facing experimental gravitation today [3]. For over four decades scientists have been actively involved in the search for gravitational waves. The detection of GWs will be a grand testimony to Albert Einstein's unfinished symphony [4]. GWs will enable us to look into the very essence of black holes and further stimulate the field of gravitational wave astronomy. Furthermore, it will open a new window onto the universe that we are so curious about. The search for GWs was pioneered by Joeseph Weber in the late 1960s. His observations have been controversial and are not a currently accepted as true. However, Weber's experimental observations and claims (to have detected GWs) have truly stimulated the monumental efforts of scientists from a variety of disciplines. The data analysis involved in the detection of GWs is truly a multidisciplinary task that draws expertise from many fields. The search for GWs has now become a global effort and research groups from the Canada, United States of America, Great Britain, France, Germany, Italy, Japan, India, Australia, and Brazil, etc, are now intensely involved in this challenge.

Both the electromagnetic and gravitational forces are long range. However, the processes theorized to drive GW emission are fundamentally different from processes that radiate electromagnetically. GW astronomy will give us a new view of the universe that is in contrast to that obtained from electromagnetic waves. In fact, the information provided by GW would be "orthogonal" [5] to that provided by electromagnetic waves. A few simple facts given below will give strong credence to the above observation:

1. EM waves are oscillations of the electric and magnetic fields that propagate through spacetime, whereas GWs are theorized to be ripples of spacetime itself [5].

2. The EM waves are produced from the incoherent superposition of emissions from individual electrons, atoms, and molecules. GWs in contrast are the coherent superposition of radiation that arises from the large size dynamics of dense sources of mass-energy. This could be either matter or even the high curvature of spacetime itself. GWs provide direct information about the dynamics of the source that generates the radiation. This is analogous to EM radiation from the Sun providing information about its constitution.

3. In general, the wavelength of EM waves is smaller than the size of the radiating system. That helps in forming images of the radiating sources/systems. This is in strong contrast to the case of gravitational radiation. In the case of GWs, the wavelength is typically predicted to be of either the order or larger than the size of the radiating system. Instead of trying to image the source, the

important point is to use the GW polarizations (there are two just like in the EM case), which are similar to sound for getting a stereophonic description of the dynamics of the source.

4. EM astronomy is founded upon deep imaging of small angle fields of observation. This way observers can get a large amount of information about sources on a small patch of the sky. In contrast, GW astronomy has to focus on an all-sky search with an active involvement of detectors such as LIGO, VIRGO, TAMA, GEO600, AIGO, and LISA. Specifically-targeted searches on a small region of the sky are only one facet of the overall search.

5. EM waves interact strongly with matter. GWs, in strong contrast, do not. This has both pros and cons. The advantage is that the GWs propagate from the emission source to the Earth with almost zero absorption. This enables one to look into the astrophysics hiding in the interior of dense astrophysical objects, as well as the dynamics of the very early universe. The disadvantage is that the GWs interact very weakly with GW detectors. As a consequence, the experimental, theoretical, and observational challenges for detecting GWs is a monumental effort.

6. One of the most important differences between EM and GW waveforms is that most EM observables can be represented as a type of energy flux, and so obey a $\frac{1}{r^2}$ law. However, for GW waveforms, as they are generally designated, the observable is the amplitude of the wave, related to the fractional strain, which falls off as $\frac{1}{r}$. Consequently, even small improvements in GW detector sensitivity will have substantial impact on the ability to make measurements. Simply put, when a detector sensitivity is doubled it essentially doubles the distances to which sources can be detected. Thereby, the volume of the region of the universe in which sources are measured will increase by a factor of 8, making the number

of sources much larger.

1.1 Overview

This thesis performs the pattern recognition technique known as matched filtering using templates for a gravitational wave data analysis. An analytic expression is derived for what is known as the inner product, which is used in the expression for the fitting factor. The fitting factor expression is studied through numerical experiments using a simulated model pulsar signal and generated templates.

1.2 Thesis objectives

The main objectives of this thesis are:

1. To apply matched filtering using templates to a GW pulsar signal model.
2. To derive an analytic expression for the inner product and fitting factor of matched filtering.
3. To develop a computer program to implement the derived analytic inner product expression.
4. To numerically explore the parameter space of the templates.

1.3 Thesis outline

The rest of this thesis is organized as follows:

Chapter two: introduces differential geometry as used in General Relativity. Gravitational waves are described mathematically and their effects on test masses demonstrated.

Chapter three: detection and measurement of a GW signal are discussed, and gravitational wave data analysis techniques are described.

Chapter four: the matched filtering technique is defined and motivated through a discussion of the maximum likelihood statistical inference idea, and spectral noise density is discussed.

Chapter five: the model GW signal and its Fourier transform are given.

Chapter six: an analytic derivation of the inner product of matched filtering using the model from chapter five is performed.

Chapter seven: numerical implementation details for a program to calculate the inner product expression from chapter six are discussed.

Chapter eight: results from numerical studies using the program from chapter seven are presented.

Chapter nine: presents conclusions and comments.

Chapter 2

Mathematical Review

GWs are ripples in spacetime geometry, and so the principles of General Relativity need to be understood. For that reason a review of differential geometry is given in this chapter. The aim is to develop the ideas that are required to reach the mathematics of the gravitational wave. Once the mathematics have been developed it will be possible to understand how a gravitational wave can be detected by a device such as a Michelson interferometer.

2.1 Pulsars

All waves have a source that emits them. In the case of gravitational waves the sources are any large masses that undergo acceleration. There are many such candidates. However, of particular interest are continuous sources from extremely magnetized rotating neutron stars named pulsars, which were discovered in 1967. Due to continuous emission of GWs by the pulsars, an enhanced signal to noise ratio can be attained through long observation times. Such an enhancement makes them more easily detectable. Also due to the large density of them in the universe they are effectively a background noise. An understanding of the gravitational waves from pulsars will lead to the ability to isolate and remove their contribution to a detected signal. Thereby, more transient sources such as black hole mergers can be studied more effectively.

The reason for studying a pulsar is that it is a prime source for continuous gravitational waves. The frequency is almost constant, as well as its source location on the sky. The frequency of the waves is known in most cases to decrease. The phenomenon is known as spindown. Mathematically the spindown is $\frac{df}{dt}$, which has units of Hz/s.

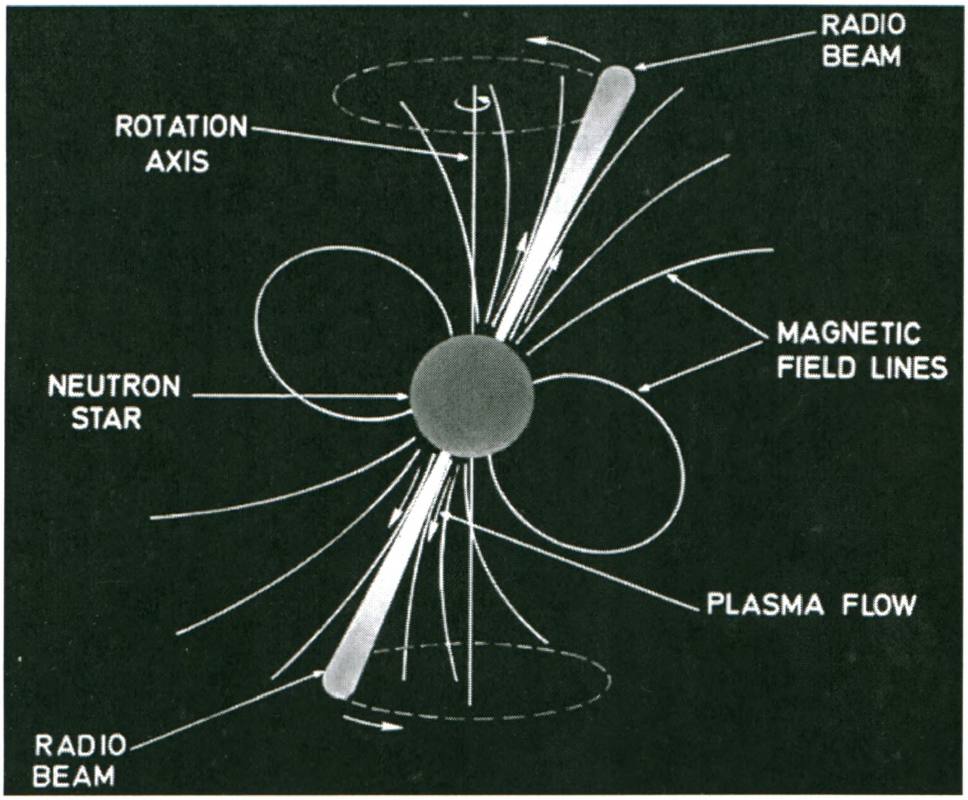

Figure 2.1: Pulsar Model Schematic [6].

2.2 Differential geometry review

Geometry is generalized through the use of differential and integral calculus, which reduces it to a specification of the distance between each pair of nearby points. The infinitesimal distances between between nearby points are summed along curves using integration. Straight lines are the curves of the shortest distance between two points. Angles are ratios of the lengths of arcs to their radii when those radii are small.

Areas, volumes, etc., can be constructed by multiple integrals over area and volume elements, themselves specified by the distances between nearby points. This area of mathematics is known as *differential geometry* [7]. These ideas are discussed in this section.

Geometry is coordinate independent, but the line element for a geometry will take different forms based on the coordinate system used. That means that more than one line element can represent the same geometry. As an example, consider Euclidean geometry. In Cartesian coordinates the line element, denoted dS, for 2-dimensional Euclidean geometry is give by the familiar Pythagorean expression

$$dS = \left[(dx)^2 + (dy)^2\right]^{1/2} \tag{2.1}$$

and in polar coordinates the line element for the same Euclidean geometry is

$$dS = \left[(dr)^2 + (rd\phi)^2\right]^{1/2} \tag{2.2}$$

The key point to understand is that the above line elements are equivalent representations of the same underlying geometry. That is, they will both give rise to identical geometrical facts, such as the circumference of a circle, and arclength. "Coordinates are just a convenient and systematic way of labeling the points in a geometry" [7]; there is nothing physical about them. The distance between nearby points is an invariant quantity with respect to the coordinates used to compute it. The previous example involved line elements describing a 2-dimensional geometry, but the fundamental idea is extendable to a n-dimensional geometry.

To describe a general n-dimensional geometry requires a coordinate system consisting of n coordinates. In General Relativity the geometry has four dimensions and is called *spacetime.* The coordinates for spacetime represent time and the three spatial dimensions. Those coordinates are commonly denoted by the symbols t, x,

y, z, but another set of symbols is used for General Relativity, which proves more convenient. The new set is x^0, x^1, x^2, x^3, where

$$x^0 \equiv t \tag{2.3}$$

$$x^1 \equiv x \tag{2.4}$$

$$x^2 \equiv y \tag{2.5}$$

$$x^3 \equiv z. \tag{2.6}$$

The new symbols allow for reference to any one of the coordinates by using the symbol x^α, where $\alpha = 0, 1, 2,$ or 3. If any other Greek index is used, then it takes on the same values as α. For example, x^β implies that $\beta = 0, 1, 2$ or 3. When a Roman index is used the index is assumed to take on the values $1, 2,$ or 3.

2.2.1 The Einstein summation convention

The equations of differential geometry often involve many summations. A close analogy is the summation involved in matrix multiplication. For instance, suppose one wishes to calculate the components of a vector, $\boldsymbol{C}$, which is equal to a 4-dimensional square matrix, $\boldsymbol{A}$, multiplied by a different 4-dimensional vector, $\vec{x}$. Then in symbols one would write

$$\boldsymbol{C} = \boldsymbol{A}\vec{x}. \tag{2.7}$$

The ith component of $\boldsymbol{C}$ is then traditionally written as

$$C_i = \sum_{j=1}^{4} A_{ij} x_j. \tag{2.8}$$

However another way is possible that saves on notation. It could also be written as

$$C_i = A_{ij}x^j, \tag{2.9}$$

using the new idea that a repeated index occurring as a superscript and subscript implies summation over that index. In General Relativity a similar idea is followed, which is called the *Einstein summation convention.* It facilitates much easier manipulation of the equations encountered in the theory. The convention is a short set of rules to follow when manipulating and writing equations, and is the following

1. The placement of indices, either upper or lower, must not change. Upper indices are used for coordinates and vector components. Lower indices are used for the metric, which is described shortly.

2. An index that occurs more than once in an equation is called a *summation index.* It is to only occur in an upper-lower pair, for example $x^\alpha y_\alpha$. A summation index implies a summation over that index. For example

$$x^\alpha y_\alpha = x^0 y_0 + x^1 y_1 + x^2 y_2 + x^3 y_3, \tag{2.10}$$

   where the summation index is α.

3. An index that is not a summation index is called a *free index.* A free index must occur on both sides of the equals sign of an equation.

2.3 General Relativity

2.3.1 The spacetime metric

The x^α are used to label points. Their differentials, dx^α, are used in the line element, ds^2, to give the distance between nearby points. That line element will have the form

$$ds^2 = g_{\alpha\beta}(x)dx^\alpha dx^\beta, \tag{2.11}$$

where $g_{\alpha\beta}(x)$ is a symmetric, position-dependent matrix called the *metric* [7]. The form of the metric will be different in different coordinate systems. The metric for the geometry of flat spacetime, expressed in cartesian coordinates, is traditionally denoted $\eta_{\alpha\beta}$, and defined to be

$$\eta_{\alpha\beta} = \begin{pmatrix} -1 & 0 & 0 & 0 \\ 0 & 1 & 0 & 0 \\ 0 & 0 & 1 & 0 \\ 0 & 0 & 0 & 1 \end{pmatrix}. \tag{2.12}$$

As an example, the line element for flat spacetime (in units where the speed of light, c, is unity), denoted $\eta_{\alpha\beta}$, is calculated as

$$\begin{aligned} ds^2 &= \eta_{\alpha\beta}dx^\alpha dx^\beta \qquad (2.13)\\ &= -(dx^0)^2 + (dx^1)^2 + (dx^2)^2 + (dx^3)^2 \qquad (2.14)\\ &= -dt^2 + dx^2 + dy^2 + dz^2 \qquad (2.15) \end{aligned}$$

where the traditional coordinate symbols are used for the last line. The line element just derived is that for *special relativity* expressed in cartesian coordinates.

2.3.2 The geodesic equation

In classical mechanics the laws of Newton are used to describe the motion and path of particles. In the absence of a net force on a particle Newton's theory says that the particle will continue along in a straight line at a constant velocity. In General Relativity there is a similar idea. The path that a free particle or light follows in spacetime is called a *geodesic.* The equation of motion for the free particle or light is called the *geodesic equation*, which is [7]

$$\frac{d^2x^\alpha}{d\tau^2} = -\Gamma^\alpha_{\beta\gamma}\frac{dx^\beta}{d\tau}\frac{dx^\gamma}{d\tau}, \tag{2.16}$$

where the *proper time*, denoted by τ, is defined by $d\tau^2 = -ds^2/c^2$. The $\Gamma^\alpha_{\beta\gamma}$ are coefficients called *Christoffel symbols*, which are implicitly defined by [7]

$$g_{\alpha\delta}\Gamma^\delta_{\beta\gamma} = \frac{1}{2}\left(\frac{\partial g_{\alpha\beta}}{\partial x^\gamma} + \frac{\partial g_{\alpha\gamma}}{\partial x^\beta} - \frac{\partial g_{\beta\gamma}}{\partial x^\alpha}\right). \tag{2.17}$$

An equivalent form of the geodesic equation can be written using the *four-velocity*, defined by $u^\alpha \equiv \frac{dx^\alpha}{d\tau}$,

$$\frac{du^\alpha}{d\tau} = -\Gamma^\alpha_{\beta\gamma}u^\beta u^\gamma. \tag{2.18}$$

The geodesic equation is analogous to Newton's second law of mechanics $F = \frac{d\vec{p}}{dt}$.

2.4 Gravitational waves

At this point the mathematics required to develop the gravitational waves has been covered. The spacetime geometry of General Relativity, the line element, the metric, and the geodesic equation will all be used in the understanding of the gravitational waves. The waves will be shown to be a perturbation of flat spacetime, to have two polarizations, and to cause distances between isolated test masses to change.

2.4.1 Linearized plane waves

The gravitational wave forms theorized by astrophysicists to be detectable on the Earth are small amplitude plane waves. The small amplitudes are because the Earth is far from GW sources such as pulsars and merging black holes, and the energy of the GWs follows an inverse square law from the source. The wave fronts are also theorized to be practically planar because, though the GWs are emitted spherically in all directions, when they reach the distant Earth the wavefronts will be immense spheres. For that reason the following mathematics is applicable in practice because it leads to GWs propagating as plane waves of small amplitude when far from the source of emission. It uses a perturbation of flat spacetime, which is what the gravitational waves essentially are when they reach the Earth.

In the region of the Earth the spacetime is practically Euclidean, which means that the metric is, to an excellent approximation, equal to that of flat spacetime, $\eta_{\alpha\beta}$. The *perturbation metric* of flat spacetime is denoted by $h_{\alpha\beta}$, which changes the total metric to be [8]

$$g_{\alpha\beta} = \eta_{\alpha\beta} + h_{\alpha\beta}. \tag{2.19}$$

The perturbation metric has a very small magnitude, $|h_{\alpha\beta}| << 1$. The preceding approximation for the metric solves the first order term resulting from the expansion of the Einstein equation in amplitude of the wave. Since the order of waves to be detected is 10^{-21} [8], the approximation is extremely accurate.

The above metric, Equation (2.19), leads to a wave equation [8]. This is why gravitational radiation is called gravitational waves. The GW wave equation is

$$\left(-\frac{1}{c^2}\partial_0^2 + \nabla^2\right)\bar{h}_{\mu\nu} = 0, \tag{2.20}$$

and implies that the speed of propagation of the GWs is that of light. This is analogous to the general wave equation for a scalar function u

$$\left(-\frac{1}{v^2}\frac{\partial^2 u}{\partial t^2} + \nabla^2\right) u = 0, \tag{2.21}$$

where v is speed of the wave and ∇^2 is the *Laplacian.* The GW wave equation has plane wave solutions. The general solution for a GW traveling in the z direction is given by

$$h_{\alpha\beta}(t,z) = \begin{pmatrix} 0 & 0 & 0 & 0 \\ 0 & f_+(t-z) & f_\times(t-z) & 0 \\ 0 & f_\times(t-z) & -f_+(t-z) & 0 \\ 0 & 0 & 0 & 0 \end{pmatrix}, \tag{2.22}$$

where $f_+(t-z)$ and $f_\times(t-z)$ are dimensionless functions that give the form of the wave. The form will vary with the source of emission. Later in this thesis the $f_+(t-z)$ and $f_\times(t-z)$ for a pulsar emission source will be given. The spacetime interval for the plane wave solution is

$$\begin{aligned} ds^2 &= g_{\alpha\beta}dx^\alpha dx^\beta && (2.23) \\ &= (\eta_{\alpha\beta} + h_{\alpha\beta})dx^\alpha dx^\beta && (2.24) \\ &= -dt^2 + [1 + f_+(t-z)]dx^2 + [1 - f_+(t-z)]dy^2 + dz^2 + 2f_\times(t-z)dxdy. && (2.25) \end{aligned}$$

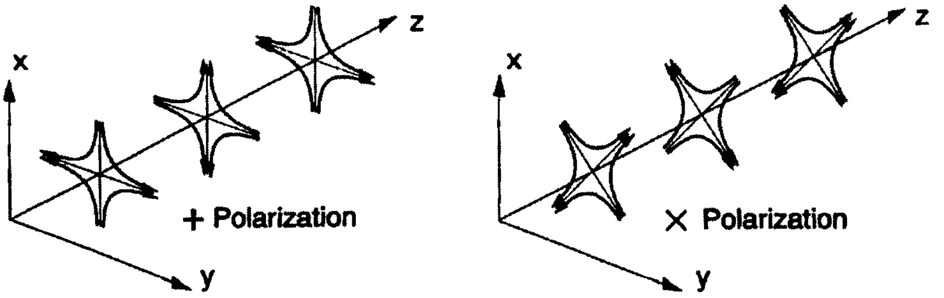

Figure 2.2: Gravitational wave polarizations [5].

2.4.2 The effect of a gravitational wave

To motivate the method for detecting and measuring a gravitational wave, the following example is given. It will be shown that the effect due to a gravitational wave is a change in distances between isolated test masses. That phenomenon is the fundamental mechanism underlying the effectiveness of interferometric devices currently built to detect gravitational waves.

Suppose that a plane gravitational wave is about to pass by the region of two isolated test masses. Define the propagation direction of the wave to be in the positive z direction. The perturbation metric is then given by Equation (2.22). Assume that before the wave passes the spacetime is flat, $\eta_{\alpha\beta}$, and that the coordinates of the masses are $x_a^i = (0,0,0)$ and $x_b^i = (L_*, 0, 0)$. The distance between them is L_*. When the wave passes by, the metric becomes that of the perturbed approximation, $g_{\alpha\beta} = \eta_{\alpha\beta} + h_{\alpha\beta}$, as discussed in the previous subsection. The distance, L, between the masses is then

$$L(t) = \int_0^{L_*} [1 + f_+(t - z)]^{1/2} dx \tag{2.26}$$

$$= [1 + f_+(t - z)]^{1/2} \int_0^{L_*} dx \tag{2.27}$$

$$\approx L_* \left[1 + \frac{1}{2} f_+(t - z)\right], \tag{2.28}$$

where the first two terms of a Taylor approximation have been kept in the last step. The distance between the masses which began as L_* has been changed by an amount depending upon the $f_+(t - z)$ component of the perturbation metric, and so it varies with time. And the component of the perturbation metric is the form of the gravitational wave. It is by observing changes in distances between test masses that the gravitational waves can be detected and then measured.

The gravitational wave component is equal to what is called the *fractional strain*. The fractional strain due to a gravitational wave is defined to be the change in length divided by the length itself. For the example just given, the fractional strain is denoted by $h(t)$ and given by

$$h(t) = \frac{L - L_*}{L_*} \tag{2.29}$$

$$= \frac{1}{2} f_+(t - z). \tag{2.30}$$

A gravitational wave detector is any device that records changes in fractional strain with time. By measuring the fractional strain, the gravitational wave itself is also being measured. It must be emphasized that the fractional strain with time is crucial in GW data analysis because analysis methods rely on it as the fundamental input. The example just given of measuring the change of distance between two isolated masses is the principle reason that modern GW detectors have *Michelson interferometer* designs (see Figure 2.3). In the next chapter the GW data analysis of a pulsar signal is discussed.

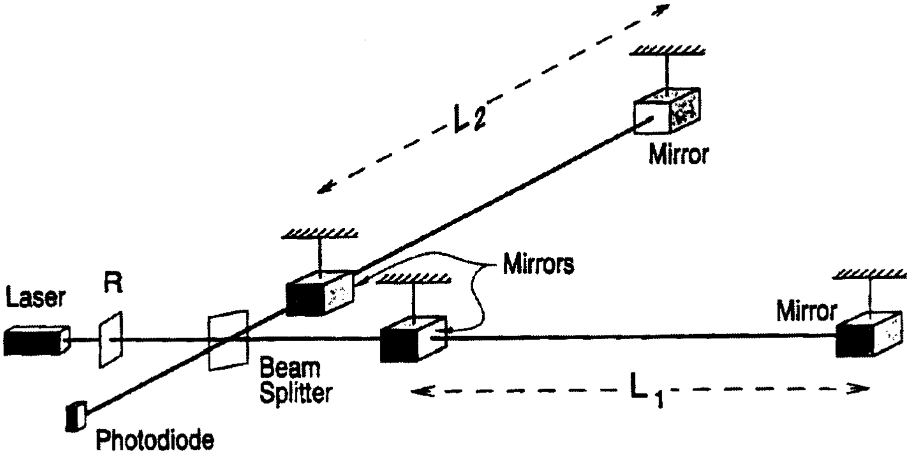

Figure 2.3: Michelson interferometer to detect GWs [5].

2.4.3 Detector equation

Any detector whose relative location from a GW source is not constant will experience a sky-position dependent Doppler effect. In the case of an Earth-bound gravitational wave detector, the effect is caused by the Earth's rotation about its axis, and its orbit about the Sun. Taking into account the Doppler effect is crucial to all of the data analysis methods to be described in the next chapter. That is the reason for explicitly including the sky position in the antenna beam pattern functions, F_+ and $F_\times$, which give the sensitivity of the detector to different GW polarizations.

A GW detector will record the fractional strain with time, $h(t)$. The antenna beam patterns are known *a priori*. The generation of $h(t)$ is theoretically a function of the known beam pattern functions, and the unknown GW polarizations, h_+ and

$h_\times$ [9] [10]:

$$h(t) \equiv F_+(t,\phi,\theta,\Psi)h_+(t) + F_\times(t,\phi,\theta,\Psi)h_\times(t) \tag{2.31}$$

where the symbols are defined as follows:

$$\phi \equiv \text{azimuthal angle of the pulsar source} \tag{2.32}$$

$$\theta \equiv \text{colatitude angle of the pulsar source} \tag{2.33}$$

$$\Psi \equiv \text{polarization angle of the pulsar source.} \tag{2.34}$$

The data analysis objective is to obtain h_+ and $h_\times$ from the known F_+ and $F_\times$ and the measured $h(t)$. This is discussed in chapters 3 and 4.

2.5 GW signal waveform for a pulsar

The relationship given by Equation (2.31) is quite general. What is needed is an an expected form of the GW polarizations, h_+ and $h_\times$. For the case of periodic GWs with elliptical polarizations, as is theoretically expected to be emitted from an isolated tri-axial rotating neutron star, the GW form is as follows [10]:

$$h_+(t) = A_+ \cos(\Phi(t)) \tag{2.35}$$

$$h_\times(t) = A_\times \sin(\Phi(t)) \tag{2.36}$$

where

$$\Phi(t) = \text{the phase of the signal at the detector.} \tag{2.37}$$

The A_+ and $A_\times$ are related to the inclination angle for the source, ι, and the wave amplitude, h_0, as follows [10]:

$$A_+ = \frac{1}{2}h_0(1+\cos^2(\iota)) \tag{2.38}$$

$$A_\times = h_0\cos(\iota). \tag{2.39}$$

The amplitude h_0 is given by [10]

$$h_0 = \frac{16\pi^2 G}{c^4}\frac{I\epsilon\nu^2}{d} \tag{2.40}$$

where

$$\nu = \text{rotational frequency} \tag{2.41}$$

$$I = \text{the principal moment of inertia about spin axis} \tag{2.42}$$

$$\epsilon = \text{equatorial ellipticity of the star} \tag{2.43}$$

$$d = \text{distance from the detector to the star.} \tag{2.44}$$

The inclination angle of the source, ι, is the angle of the pulsar spin axis with respect to the line of sight between the source and detector [10].

Chapter 3

Gravitational Wave Data Analysis

In this chapter gravitational wave data analysis is presented. General concepts such as the difference between detection and measurement of a gravitational wave are given, and specific techniques to accomplish both are studied.

Theoretical models for the shape of a GW signal from a pulsar are known [11] [12]. The models typically have a finite number of parameters whose values specify the properties of the pulsar source. An instance of a given model will be defined when its parameter set is specified by giving each parameter a value. The set of parameters is most commonly taken to be the pulsar location on the sky, its frequency, and its spindown parameters [13].

3.1 Detection and measurement

The distinction between the separate concepts of detection and measurement of a GW signal has to be kept clear [14]. Detection is the observation that a GW signal modified the strain of a detector and so gave rise to a change in its time series. It is a statistical question in nature and so answered with a probability value. Measurement, on the other hand, necessarily follows detection. It fundamentally assumes that a signal is present. It then measures the parameter values giving rise to the signal. These ideas rely heavily on the general mathematical ideas developed in [15] on how to extract a signal from noise. The ideas in [15] are thoroughly applied in the context of gravitational waves by Finn [14].

Given a detector response, $g(t)$, either a signal is present or it is not. If the noise of the detector is assumed to be white and Gaussian, $n(t)$, then the detector response is [14]

$$g(t) = \begin{cases} n(t) & \text{when no signal is present} \\ n(t) + m(t;\lambda) & \text{when a signal is present,} \end{cases} \tag{3.1}$$

where $m(t;\lambda)$ is the pulsar signal generated by the set of parameters denoted collectively by λ. It is found that the probability of detection, $P(m|g)$, is given by

$$P(m|g) = \frac{\Lambda}{\Lambda + P(0)/P(m)}, \tag{3.2a}$$

where

$$\Lambda \equiv \int d^N\mu \Lambda(\mu), \tag{3.2b}$$

$$\Lambda(\mu) \equiv p(\mu)\frac{P[g|m(\mu)]}{P(g|0)}. \tag{3.2c}$$

Equation (3.2a) relies on three *a priori* probabilities, and the ratio of two conditional probabilities [14]:

1. $P(0)$ the *a priori* probability that the signal is *not present.*
2. $P(m)$ the probability density of observing $g(t)$ in the absence of the signal.
3. $p(\mu)$ the probability density of observing $g(t)$ assuming $m(t;\mu)$ with *particular* μ is present.
4. $\frac{P(m|g)}{P(0|g)}$.

Setting the *a priori* probabilities to expected forms, and substituting into Equations (3.2), gives the probability of detection. This is the detection step, and precedes measurement of the GW pulsar parameters.

Measurement is the determination of the parameter values of the emitting GW source. The domain of the problem lies in the realm of pattern recognition. A suitable pattern recognition technique is required in order to extract the pulsar signals that are embedded in the noise of the detector. The data analysis technique employed in this thesis for such a purpose is referred to as matched filtering using templates. It relies on an *a priori* model of a pulsar signal. However, different measurement techniques are found in the literature. A brief outline of the popular methods is given in the next section. Matched filtering itself is thoroughly discussed in chapter 4.

3.2 Data analysis methods

There are two kinds of *search types*:

1. *directed* - a specific search for a suspected well known source, such as the Crab or Scorpius X-1 pulsars.

2. *all-sky* - a parameter space search, where the source is unknown.

There are two kinds of *analysis types*:

1. *coherent* - a continuous segment of time series.

2. *incoherent* - disconnected segments of time series.

The directed search can be thought of as an instance of the all-sky search where the parameter space is reduced completely to a single sky location. A directed search is possible because pulsars are detected with radio telescopes, which can provide extremely accurate sky locations. Also, the pulsar's pulses can be used to theoretically infer the possible GW frequencies emitted by the source. In that way, a data analysis can be performed to look at a specific source for GWs so that limited computational resources can be applied solely to that goal, maximizing their pattern recognition potential.

An all-sky search is more interesting because part of its parameter space covers the sky location parameters of a pulsar. The parameter space consists of all those parameters that parameterize a pulsar model. For this thesis the parameters studied are the pulsar's sky location and its frequency. In the literature another set are the pulsar spindown parameters, which are the rates of change of its pulsing frequency.

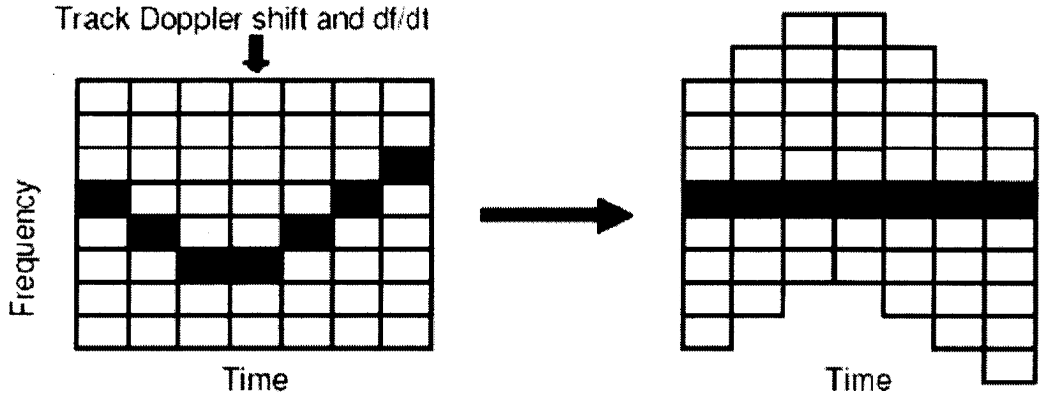

Figure 3.1: "An illustration of the discrete frequency bins of the short Fourier transform (SFTs) of the data are shown vertically, with the discrete start times of the SFTs shown horizontally. The dark pixels represent a signal in the data. Its frequency changes with time due to Doppler shifts and intrinsic evolution of the source. By sliding the frequency bins, the power from a source can be lined up and summed after appropriate weighting or transformation. This is, in essence, the starting point for all of the semicoherent search methods presented here, though the actual implementations differ significantly" [10].

Some *analysis methods* found in the GW literature are the following:

1. StackSlide
2. Tomographic reconstruction
3. Hough transform
4. Power-flux sums weighted SFT power
5. Hough sums weighted binary counts
6. Matched filtering (see chapter 4)

Chapter 4

Matched Filtering using Templates

The gravitational wave analysis method used in this thesis is known as matched filtering using templates. At its heart is a technique known as maximum likelihood estimation. In this chapter the estimation technique will be discussed, followed by the matched filtering method and associated lattice coverings.

4.1 Maximum likelihood estimation

The central idea behind the matched filtering pattern recognition technique is the statistical inference method named *maximum likelihood estimation.* It was pioneered by Sir R. A. Fisher from 1912 to 1922 [16]. The method provides a means to determine the most likely values of *model parameters* of a statistical model that give rise to a set of observations. It uses an assumption that is known as the *likelihood principle* in statistics. The principle is that the set of model parameter values that maximize the probability of a set of observed outcomes will best estimate the values of the true model parameters used to generate those same outcomes. Maximum likelihood estimation usage is quite common and used in innumerable branches of science, as well as in other fields of knowledge.

The *likelihood* is a function of the parameters defining a chosen statistical model whose form is known. Whereas *a priori* probability is used in a statistical model to deduce likely outcomes of an experiment, likelihood is used to infer the most likely model parameters giving rise to an observed set of outcomes. The *likelihood function* is defined in terms of a statistical model's probability density functions, $f(x|\theta)$, to be

$$L(\theta|x) \equiv f(x|\theta), \tag{4.1}$$

where θ is a continuous model parameter and x represents an observed outcome.

Suppose that n independent observations are made of the variable x, giving rise to the observations x_j where $j = 1 \ldots n$. Then the likelihood is

$$L(\theta|x) = f(x_1|\theta)f(x_2|\theta)\cdots f(x_n|\theta). \tag{4.2}$$

The log of the likelihood, Equation (4.2), is then

$$\ln(L(\theta|x)) = \ln(f(x_1|\theta)) + \ln(f(x_2|\theta))\cdots\ln(f(x_n|\theta)). \tag{4.3}$$

The value of the model parameter θ that maximizes Equation (4.3) will also maximize Equation (4.2) because the logarithm is a monotonically increasing function. The logarithmic transformation is convenient because it replaces multiplications with the easier to handle additions.

A method to find the maximum of Equation (4.3) begins by setting its derivative equal to zero

$$\frac{d\ln(L(\theta|x))}{d\theta} = 0 \tag{4.4}$$

and then solving for the zeros of the derivative. Then a maximum will result for a zero that gives a negative second derivative of Equation (4.3). The value for the model parameter θ where Equation (4.3) maximizes the likelihood is taken be the most likely value for the model parameter giving rise to the observations. A greater number of observations will lead, in general, to a better estimate of θ. This is where the *maximum likelihood principle* is assumed to be true.

4.2 Matched filtering using templates

Matched filtering is a pattern recognition technique. The core idea behind it is maximum likelihood estimation which is described in section 4.1. In this thesis matched filtering is applied to a detector time series in order to recognize the pattern induced by a GW pulsar signal. The estimation technique requires a statistical model. The statistical model that is chosen is the pulsar signal model described in section 2.5. The pulsar model involves many parameters, however in this study the set of model parameters is $\{\theta,\ \phi,\ f_0\}$, where

$$\theta \equiv \text{is the colatitude angle of the pulsar} \tag{4.5}$$

$$\phi \equiv \text{is the azimuthal angle of the pulsar} \tag{4.6}$$

$$f_0 \equiv \text{is the GW frequency of the pulsar.} \tag{4.7}$$

The chosen set of parameters to study are the most important because they influence the pattern in the time series to a greater extent than do the others, such as spindown and ellipticity.

A *template* [17] is defined to be an instance of a pulsar model. That is, a pulsar model with given values for its parameters, for instance $\phi = 29$ degrees, $\theta = 98$ degrees, and $f_0 = 579$ Hz. The maximum likelihood method is applied to a set of templates that differ in their parameter values. The parameter values that give the greatest likelihood are then assumed to be closest to those of the actual pulsar. The value that is sought to be maximized is termed the *fitting factor* [17], which is defined in section 4.2.2. The fitting factor definition involves the *inner product* [18] defined in section 4.2.1. A set of templates is referred to as a *family of templates.* The choice of a template family is referred to as a *lattice covering.* These terms are defined and described in the following sections, and applied in chapters 6 and 8.

4.2.1 The inner product

The matched filtering analysis relies primarily on the definition of the *inner product* of two functions, denoted $(h_1|h_2)$. In the GW pulsar related literature, maximum likelihood estimation was first applied by Jaranowski et al [9]. In that paper the authors assumed that the spectral noise density, $S_h(f)$, is constant (white noise). They derived a formula for a ratio of likelihoods, Λ, in terms of Equation (4.9) to be

$$\ln \Lambda = \frac{T}{S_h}\left[(x||h) - \tfrac{1}{2}(h||h)\right], \tag{4.8}$$

where they defined their inner product, $(x||y)$, to be

$$(x||y) \equiv \frac{2}{T}\int_{-T/2}^{T/2} x(t)y(t)dt, \tag{4.9}$$

where

$$S_h \equiv \text{is the one-sided spectral noise density} \tag{4.10}$$

$$T \equiv \text{is the time interval of observation} \tag{4.11}$$

$$x \equiv \text{is a time series} \tag{4.12}$$

$$y \equiv \text{is another time series (possibly equal to } x\text{).} \tag{4.13}$$

The definition of the inner product used in this thesis is given by Cutler and

Flanagan [18]

$$(h_1(t)|h_2(t)) \equiv 2\int_0^\infty \frac{\tilde{h}_1^*(f)\tilde{h}_2(f)+\tilde{h}_1(f)\tilde{h}_2^*(f)}{S_n(f)}df \tag{4.14a}$$

$$= \int_{-\infty}^\infty \frac{\tilde{h}_1^*(f)\tilde{h}_2(f)+\tilde{h}_1(f)\tilde{h}_2^*(f)}{S_n(f)}df \tag{4.14b}$$

$$= \int_{-\infty}^\infty \frac{2\Re\left(\tilde{h}_1^*(f)\tilde{h}_2(f)\right)}{S_n(f)}df. \tag{4.14c}$$

Where $\tilde{h}_1(f)$ and $\tilde{h}_2(f)$ are the Fourier transforms of $h_1(t)$ and $h_2(t)$, respectively. A superscript $*$ denotes complex conjugation. A $\tilde{}$ denotes a Fourier transformed function. The inner product is invariant with respect to an interchange of $h_1(t)$ with $h_2(t)$.

The great benefit of using the inner product of Equation (4.14c) is that it is in terms of frequency, and so can utilize the spectral noise density of a GW detector. This is fundamentally different than the inner product expression of Equation (4.9), which is in terms of time and so cannot utilize the very important spectral noise density. The two inner product definitions are in different domains, time and frequency, which can be related through the Fourier transform.

4.2.2 The fitting factor

The term *Fitting Factor* (FF), coined by Apostolatos [17], also termed the *normalized correlation* by Balasubramanian and Dhurandhar [19], is a scalar measure ranging from 0 to 1 of how well two functions match, taking into account spectral noise density through the inner product formula, Equation (4.14). The definition of the FF is given by [17]

$$\mathrm{FF}(\theta,\phi,f_0) \equiv \frac{(h_S(t)|h_T(t;\theta_T,\phi_T,f_0))}{\sqrt{(h_T(t;\theta_T,\phi_T,f_0)|h_T(t;\theta_T,\phi_T,f_0))(h_S(t)|h_S(t))}}. \tag{4.15}$$

where a subscript T means the symbol belongs to the template and a subscript S means the symbols belongs to the signal. That is, $h_S(t)$ is the source signal and $h_T(t)$ is a template function. The FF is used determine how well a signal and a given pulsar template match. By trying many templates it is likely that a close match to the signal will be found. The larger the template family, the more likely an FF will be found that is close to the optimal value of 1.

The FF satisfies the Cauchy-Schwartz inequality. This is seen by multiplying both sides of Equation (4.15) by its denominator to find

$$(h_S(t)|h_T(t;\theta_T,\phi_T,f_0)) = \sqrt{(h_T(t;\theta_T,\phi_T,f_0)|h_T(t;\theta_T,\phi_T,f_0))(h_S(t)|h_S(t))} \tag{4.16}$$

$$\leq 1, \tag{4.17}$$

where the last step uses the Cauchy-Schwartz inequality. Based on the inequality, a FF has a value of 1 only when the template perfectly matches the pulsar signal. That is, when $h_S(t) = h_T(t;\theta_T,\phi_T,f_0)$.

For the case of the advanced LIGO noise spectrum an $FF < 0.9$ corresponds to a 27% reduction in the event rate of the relevant signals; therefore a family of templates that leads to FF's below 0.9 should be considered inadequate [17], which the results presented in chapter 8 of this thesis support.

4.3 The spectral noise density

The spectral noise density of Equation (4.14c), denoted $S_n(f)$, plays a crucial role in the performance of the template. The French-Italian VIRGO[1] GW detector is

---

[1] http://www.virgo.infn.it/

expected to have a spectral noise density given by [2]

$$S_n(f) = v_0 f^2 + v_1 + v_2 \frac{1}{f} + v_3 \frac{1}{f^5}, \tag{4.18}$$

where (in appropriate dimensions) the constants are $v_0 = 3.8 \cdot 10^{-51}$, $v_1 = 9.5 \cdot 10^{-46}$, $v_2 = 1.6 \cdot 10^{-43}$, and $v_3 = 8.3 \cdot 10^{-37}$. Considering the GW frequency range 200 Hz to 1000 Hz, of particular interest for pulsars, the extremal range values and the average are found to be the following:

$$S_n(200) \approx 1.5 \cdot 10^{-46} + 9.5 \cdot 10^{-46} + 8 \cdot 10^{-46} + 2.6 \cdot 10^{-48} \tag{4.19a}$$

$$\approx 1.9 \cdot 10^{-45}. \tag{4.19b}$$

$$S_n(1000) \approx 3.8 \cdot 10^{-45} + 9.5 \cdot 10^{-46} + 1.6 \cdot 10^{-46} + 8.3 \cdot 10^{-52} \tag{4.20a}$$

$$\approx 4.9 \cdot 10^{-45}. \tag{4.20b}$$

The average spectral noise density, $\langle S_n(f) \rangle$, is

$$\langle S_n(f) \rangle = \frac{1}{980} \int_{20}^{1000} S_n(f) df \tag{4.21a}$$

$$= \frac{1}{980} \int_{20}^{1000} \left(v_0 f^2 + v_1 + v_2 \frac{1}{f} + v_3 \frac{1}{f^5} \right) df \tag{4.21b}$$

$$= \frac{1}{980} \left(\frac{v_0}{3} f^3 + v_1 f + v_2 \ln(f) - \frac{v_3}{4f^4} \right) \Big|_{20}^{1000} \tag{4.21c}$$

$$= 1.3 \cdot 10^{-45} + 9.5 \cdot 10^{-46} + 6.4 \cdot 10^{-46} + 2.1 \cdot 10^{-52} \tag{4.21d}$$

$$= 2.9 \cdot 10^{-45}. \tag{4.21e}$$

---

[2] Dr. Tania Regimbau of the VIRGO group

The constant term, v_1, of the spectral noise density gives roughly similar contribution to the first and third terms of Equation (4.18). Therefore, in the following sections of this paper $S_n(f) = M$, where M is a real-valued constant.

In the gravitational wave data analysis literature, the spectral noise density for optimum matched filtering is generally taken to be a constant. However, considering the colored noise is informative as well as illustrative. It is found that the inner product, Equation (4.14c), and hence the FF, Equation (4.15), has an analytic solution for at least the cases when the VIRGO spectral noise density, Equation (4.18), is equal to:

1. $v_0 f^2$,
2. the constant term, v_1,
3. $\frac{v_2}{f}$,
4. $v_1 + \frac{v_2}{f}$,
5. $\frac{v_3}{f^5}$.

The general analysis will be shown in a forth-coming publication of ours. Also, it should be noted that the analysis for the LIGO and GEO 600 spectral noise densities can be done in a similar manner, paying due attention to their different forms.

A concise form of the spectral noise density that incorporates important quantum effects due to the Heisenberg uncertainty principle is given by [8]

$$S_n(f) = \frac{1}{(L\pi f_0)^2} \frac{\hbar}{M} \left[\left(1 + \frac{f^2}{f_p^2} \right) + \frac{f_0^4}{f^4} \frac{1}{(1 + f^2/f_p^2)} \right] \tag{4.22}$$

where the following definitions apply: M is the mass of the mirror of the GW laser interferometer, L is the length of each interferometer arm, f_0 is obtained by finding the optimal value of the power associated with the interferometer beam (e.g. f_0 is from 10 to 100 Hz), f_p is the so-called *pole frequency*, and $\hbar$ is Planck's constant. In the case of LIGO, $f_p \approx 90$ Hz and $L = 4$ km, while in the case of VIRGO $f_p \approx 500$ Hz and $L = 3$ km.

For continuous-wave (CW) searches it is assumed that the $FF = 1$, contrary to inspiral searches where the waveform is somewhat unknown. The family of signal-waveforms is well known and such signals lie within the template-manifold. One can always find at least one template with $FF = 1$ (i.e. perfect matched-filtering). Generally one is more interested in the related question of how much SNR is lost when there is a signal in parameter-space point λ_s and a position λ_t is targeted.

Colored noise, although considered, is not much of a worry in this analysis due to the CW signals considered having very narrow bands. In a local region around the signal-frequency, the noise is assumed to be roughly white. Furthermore the GW data is normalized in the frequency-domain by the Power Spectral Density (PSD), thereby effectively whitening the data before a search is performed.

The inner product, Equation (4.14c), with a varying (colored) spectral noise density, representative of the VIRGO GW detector, given by Equation (4.18), degrades the FF due to the additional frequency terms. It is reassuring to note that varying colored noise can be analyzed to a fairly good analytic approximation with the use of reciprocal Eulerian gamma function templates. Such templates have the valuable characteristics of the weighted trigonometric functions which facilitate such an analysis. This is not only an important mathematical and computational problem, but also of great relevance in signal processing.

4.4 The lattice covering

The *template bank*, denoted by T, is defined to be the set of templates used for matched filtering [20]. The number of templates comprising the template bank is prac-

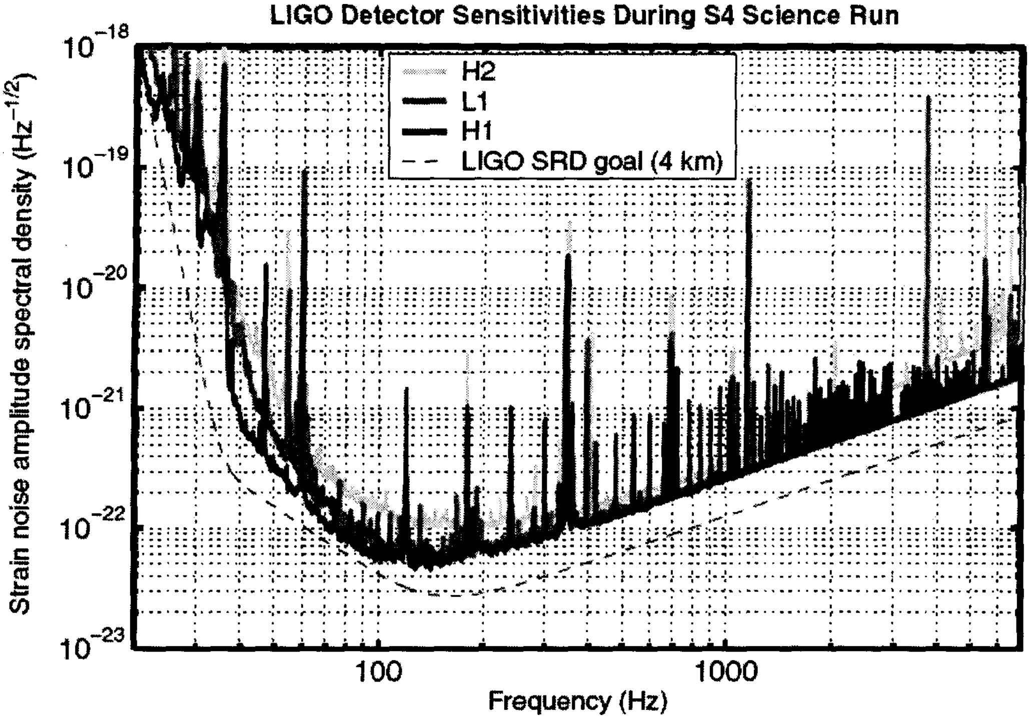

Figure 4.1: Median amplitude strain noise spectral densities from the three LIGO interferometers during the S4 run, along with the initial LIGO design sensitivity goal [10].

tically constrained by finite computational resources. To maximize those resources an efficient *lattice covering* of the parameter space is desired. A lattice covering is the arrangement of templates in the parameter space of the pulsar model. The idea is to pick a lattice covering such that a template constituting the closest match to a signal will not *mismatch* by more than a desired amount. A more stringent mismatch criteria, that is, a lower tolerance of mismatch, will necessarily increase the size of the template bank. Studies of lattice coverings have shown that the problem of choosing an efficient template bank is far from trivial [20] [21] [22].

The numerical analysis performed in this thesis, chapter 8, uses a *regular* lattice covering in the two-dimensional parameter space of the pulsar sky location. That is, the template family is a set of sky locations $\{\phi, \theta\}$, that form a uniform lattice over the entire parameter space. At the same time it takes the template parameter f_0 to be equal to that of the signal, which reduces the parameter space to two dimensions and allows for the plotting of the FF values obtained in simulations. Choosing such a regular lattice covering has more than one benefit. The first is ease of implementation in terms of computer programming, and the second is in the efficient re-use of previously computed FF values. The algorithm for generating the lattice covering is the following:

1. The first lattice, stage 1, is the template family $T = \{(0,0),\ (360,0),\ (0,180),\ (360,180)\}$, where each member represents a different (ϕ, θ) parametrization.
2. Then, for each subsequent stage, points are added to the template family, T, at the horizontal and vertical midpoints of the previous stage's points, as well as the very center.

The regular lattice coverings that result from an application of the above algorithm are shown in Figure 4.2.

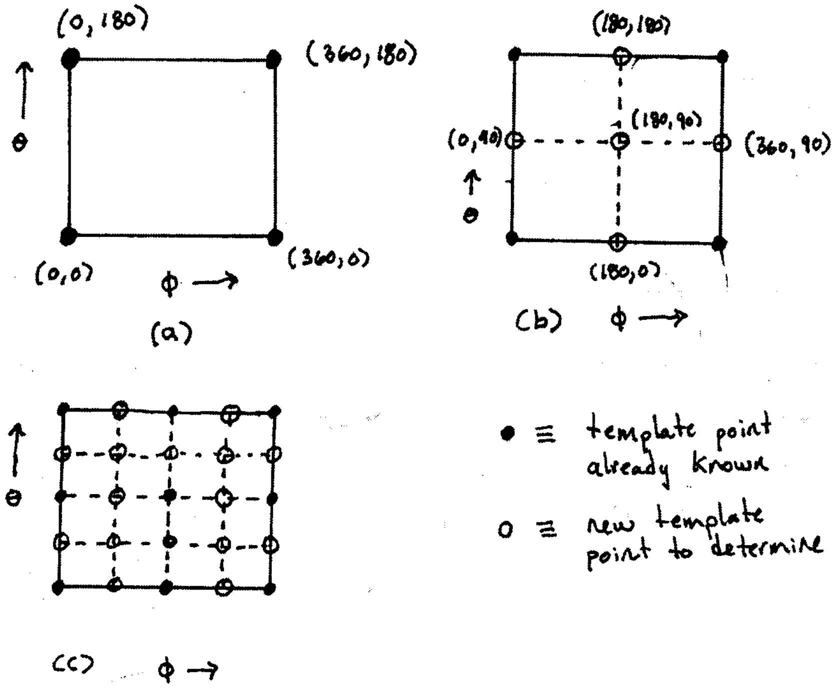

Figure 4.2: Three stages of the lattice partition algorithm. a) The first stage consisting of four points at the extreme values of the angle parameters. b) The second stage where points are added to the midpoints of the first stage, (a). c) The third stage where points are added to the midpoints of the second stage, (b). For subsequent stages the pattern repeats itself. At each stage the lattice is a uniform grid over the model parameters ϕ and θ.

Applying more stages of the algorithm will result in a larger template family, T. The regular lattice algorithm generates a different sized template family, denoted $||T(s)||$, for each stage, s. The relationship between $||T(s)||$ and s is the following

$$||T(s)|| = (1 + 2^{s-1})^2 \qquad \text{for } s = 1, 2, \ldots \tag{4.23}$$

Table 4.1 lists sizes of the template families for $s = 1, 2, \ldots, 10$. For this thesis the lattice stages chosen where either $s = 6$ or $s = 7$ due to the computational resources available.

Increasing the template family size will decrease the maximum possible mismatch, but will also increase the computational requirements. Each stage is a regular lattice that contains points of all previous stages. In this way, recalculation of FFs is eliminated. That is, FFs can be calculated for a given stage and if the maximum FF found is not high enough then the algorithm can be applied to generate new templates. However, not all members of the resulting template family will need to have their FF calculated because they are known from the previous stage. The algorithm for changing the lattice covering is closely related to the data tree structure termed a *quadtree* in computer science [23].

The regular lattice algorithm just described is not affected by any information provided through FF values of previous stages. That is, the resulting lattice coverings are predictable. This is in contrast to an *adaptive mesh* algorithm.

An adaptive mesh utilizes information from a previous stage when deciding where to place the new points. The resulting lattice covering is not generally regular. Such methods have been proposed as part of hierarchical search strategies [24]. The idea is to put a new template point only around previous templates points that are *possible candidates.* By possible candidates is meant those points whose FF values were above some predetermine threshold. It is found in [24] that three stages are significantly better than one or two, but that there is no significant benefit in using more stages.

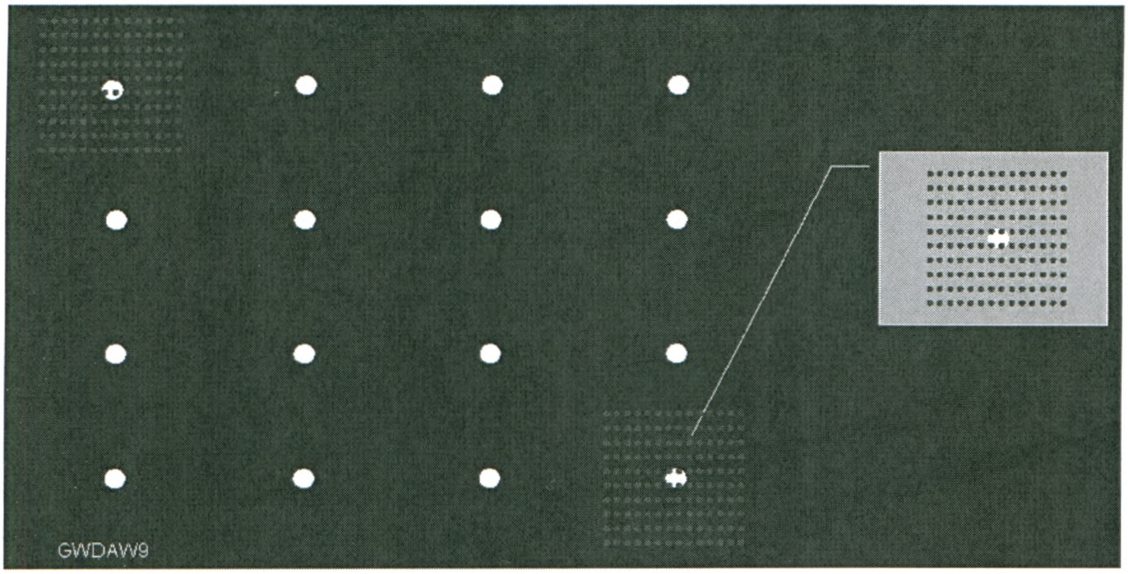

Figure 4.3: Adaptive search example. The larger dots represent templates of the previous stage, and the smaller dots represent templates of the current stage. The smaller dots are only placed around templates that are above a chosen fitting factor threshold [24].

4.5 Summary of the analysis method

In summary, after a GW pulsar signal is detected, the model parameters generating that pulsar signal are measured. The measurement is performed by the pattern recognition technique known as matched filtering using templates. The model parameters for this thesis are the sky location and frequency of a pulsar. A set of candidate templates are constructed by instances of the pulsar model parameters using the lattice algorithm of section 4.4. The observed signal is then compared with each of the templates using the fitting factor formula of Equation (4.15). The values parameterizing the template that gives rise to the largest fitting factor value are assumed to the most likely values for the true pulsar parameters based on the maximum likelihood principle.

Table 4.1: List of template family sizes for stages of the regular lattice algorithm used in this thesis. The relationship between the size of a template, $||T(s)||$, and the stage, s, is given by Equation (4.23).

Stage, s	**Template family size, $\|\|T(s)\|\|$**
1	4
2	9
3	25
4	81
5	289
6	1089
7	4225
8	16641
9	66049
10	263169

Chapter 5

The Model GW Signal

The matched filtering method requires a model of the GW signal from a pulsar. This thesis uses the model that was developed by Valluri et al. [11]. It accounts for the Doppler shift due to the rotational and orbital motion of the Earth. The frequency modulated (FM) output of the GW signal, denoted as $h(t)$, is expressed by

$$h(t) = \cos(\phi(t)) = \Re(e^{i\phi(t)}), \tag{5.1}$$

where the phase, $\phi(t)$, is given by

$$\phi(t) = 2\pi \int_{t_0}^{t} f_{received}(t')dt' = 2\pi f_0 \int_{t_0}^{t} \left(1 + \frac{\vec{v}\cdot\vec{n}}{c}(t')\right) dt', \tag{5.2}$$

where $\vec{n} \equiv (\sin\theta\cos\phi, \sin\theta\sin\phi, \cos\theta)$ is the unit vector from the solar system barycenter (SSB) origin to the pulsar, c is the speed of light (and of the gravitational wave), f_0 is the frequency of the emitted GW signal, and v is the velocity vector of the Earth in the SSB frame. It is assumed without loss of accuracy that $t_0 = 0$. $\frac{\vec{v}\cdot\vec{n}}{c}(t')$ is the total Doppler Shift at time t' due to the rotational and orbital motion of the Earth in the SSB frame.

The pulsar signal waveform, Equation (5.1), is for a h_+ polarization. The amplitude modulation (AM) is set to constant, and equal to unity. The neglected $\sin(\phi)(t)$ occurs for a $h_\times$ polarization. It is emphasized that the Fourier transform of the $h_\times$ polarization GW signal can be done exactly in the same way. For convenience in the matched filtering analysis of chapter 4, only one specific polarization type has been focused on in this study. With the inclusion of the F_+ and $F_\times$ beam pattern terms, the whole analysis is mathematically tractable, though far more complex. The study of which is of interest only if one wishes to focus on the amplitude modulation of the GW pulsar signal.

5.1 The Fourier transform of the model signal

To facilitate use of the Fourier transform result of [11], a few definitions are made. Define $h_+(t) = e^{+i\phi(t)}$ and $h_-(t) = e^{-i\phi(t)}$. Then

$$h(t) = \frac{1}{2}\left(e^{i\phi(t)} + e^{-i\phi(t)}\right) = \frac{1}{2}(h_+(t) + h_-(t)).$$

The Fourier transforms of $h_+(t)$ and $h_-(t)$ are denoted as $H_+(f)$ and $H_-(f)$, respectively. It is the case that $H_-(f) = H_+^*(-f)$. It follows that the Fourier transform of the pulsar signal $h(t)$ is

$$H(f) = \frac{1}{2}\left(H_+(f) + H_+^*(-f)\right), \tag{5.3}$$

which is the form that is used in the derivation of the inner product between a GW signal from a pulsar and a template.

The Fourier transform of Equation (5.1) is given in Valluri et al.[11]. In their derivation they use a *plane-wave expansion in spherical harmonics* [25], and manipulations of the special functions of mathematical physics to derive the following expression for the Fourier transform of Equation (5.1)

$$H_{+}(f) = \sum_{\substack{-\infty\leq n\leq\infty \\ 0\leq l\leq\infty \\ -l\leq m\leq l}} \frac{\pi^{\frac{5}{2}}\sqrt{32}}{w_r}\frac{k^{l+\frac{1}{2}}}{4^{l}} \tag{5.4a}$$

$$\cdot\, e^{-\imath\left(\frac{2\pi f_0 A}{c}\sin\theta\cos\phi+n(\phi-\frac{\pi}{2})-\frac{\pi}{2}l\right)}e^{\imath m\phi} \tag{5.4b}$$

$$\cdot\, N_{lm}^{2}P_l^{|m|}(\cos(\theta))P_l^{|m|}(\cos(\alpha))J_n(\tfrac{2\pi f_0 A\sin\theta}{c}) \tag{5.4c}$$

$$\cdot\, \frac{\Gamma(l+1)}{\Gamma\left(l+\frac{3}{2}\right)\Gamma\left(\frac{l+B_{orb}+2}{2}\right)\Gamma\left(\frac{l-B_{orb}+2}{2}\right)} \tag{5.4d}$$

$$\cdot\, {}_1F_3\left(l+1;l+\tfrac{3}{2},\tfrac{l+B_{orb}+2}{2},\tfrac{l-B_{orb}+2}{2};\tfrac{-k^2}{16}\right) \tag{5.4e}$$

$$\cdot\, \frac{1-e^{\imath\pi(l-B_{orb})R}}{1-e^{\imath\pi(l-B_{orb})}}e^{-\imath\frac{\pi}{2}B_{orb}}. \tag{5.4f}$$

Note that the exponential fraction of Equation (5.4f) is exactly analogous to the von Laue crystal diffraction pattern that arises in X-ray scattering.

The following definitions apply to the previous expression:

$$w_r \equiv Rw_{orb} \quad (R = 365,\text{ corresponding to approximately 1 year}), \tag{5.5}$$

$$B_{orb} \equiv 2\left(\frac{w-w_0}{w_r}+\frac{m}{2}+\frac{n}{2}\frac{w_{orb}}{w_r}\right) \tag{5.6}$$

and

$$k \equiv \frac{4\pi f_0 R_E\sin\alpha}{c}. \tag{5.7}$$

w_{orb} is the orbital revolution rate of the Earth about the Sun, w_r is the rotation rate of the Earth, $w_0 \equiv 2\pi f_0$ is the angular frequency of the source signal f_0, A is the distance from the center of the SSB frame to the center of the Earth, R_E is the radius of the Earth, α is the colatitude of a gravitational wave detector on the surface of the Earth and would have different values for different detectors such as LIGO and

VIRGO, θ is the polar angle, ϕ is the azimuthal angle, and N_{lm} are the normalization coefficients,

$$N_{lm} \equiv \sqrt{\frac{(2l+1)}{4\pi}\frac{(l-|m|)!}{(l+|m|)!}}. \tag{5.8}$$

The definitions of the special functions of mathematical physics used in this paper are as follows: The *gamma function*, denoted by $\Gamma(z)$, is defined as

$$\Gamma(z) \equiv \int_0^\infty e^{-t} t^{z-1} dt, \tag{5.9}$$

(with analytic continuation over the complex plane). A useful property is $\Gamma(n+1) = n!$ when n is a positive integer. The *Bessel function*, denoted by $J_m(x)$, is defined as

$$J_m(x) \equiv \sum_{r=0}^{\infty} \frac{(-1)^r}{r!\Gamma(m+r+1)} \left(\frac{x}{2}\right)^{m+2r}, \tag{5.10}$$

where m is an integer. The *associated Legendre function*, denoted by $P_l^{|m|}(x)$, is defined for a positive integer m as

$$P_l^{|m|}(x) \equiv (-1)^m (1-x^2)^{m/2} \left(\frac{d}{dx}\right)^m P_l(x), \tag{5.11}$$

where $P_l(x)$ denotes the *Legendre polynomial* defined as

$$P_l(x) \equiv \frac{1}{2^l l!} \left(\frac{d}{dx}\right)^l (x^2-1)^l, \tag{5.12}$$

where l is an integer. The *generalized hypergeometric function*, denoted by ${}_1F_3(a;b,c,d;z)$, is defined in terms of the gamma functions as

$$ {}_1F_3(a;b,c,d;z) \equiv \frac{\Gamma(b)\Gamma(c)\Gamma(d)}{\Gamma(a)} \cdot \sum_{p=0}^{\infty} \frac{\Gamma(a+p)}{\Gamma(b+p)\Gamma(c+p)\Gamma(d+p)} \frac{z^p}{p!}. \tag{5.13}$$

5.2 Reexpression of $H_+(B_f)$

To facilitate the derivation of the inner product in the next section, Equation (5.4) needs to be reexpressed into an equivalent, yet more convenient, form. This is carried out in the following subsections.

The argument of H_+ has changed from being denoted as f to B_f, which is a frequency dependent term to be defined in the next subsection. It is a more convenient and intuitive notation for use in the subsequent mathematics.

5.2.1 The exponentials

We begin our re-expression with the exponential terms of Equation (5.4f)

$$\frac{1-e^{\imath\pi(l-B_{orb})R}}{1-e^{\imath\pi(l-B_{orb})}}e^{-i\frac{\pi}{2}B_{orb}}$$

Applying the finite geometric series formula, Equation (5.4f) is

$$=\sum_{j=1}^{R} e^{\imath\pi(l-B_{orb})(j-1)}e^{-i\frac{\pi}{2}B_{orb}}=\sum_{j=1}^{R} e^{\imath\pi(j-1)l}e^{\imath\pi\left(\frac{1}{2}-j\right)B_{orb}} \tag{5.14a}$$

and after expanding B_{orb} we find

$$=\sum_{j=1}^{R} e^{\imath\pi(j-1)l}e^{2\imath\pi\left(\frac{1}{2}-j\right)B_{mn}}e^{2\imath\pi\left(\frac{1}{2}-j\right)B_f}, \tag{5.14b}$$

where

$$B_{orb}=2B_f+2B_{mn} \tag{5.15}$$

by introduction of the definitions

$$B_f \equiv \frac{w}{w_r} = \frac{2\pi f}{w_r} \tag{5.16}$$

$$B_{mn} \equiv \frac{m}{2} + \frac{n}{2}\frac{w_{orb}}{w_r} - \frac{w_0}{w_r}. \tag{5.17}$$

5.2.2 The generalized hypergeometric function

Equation (5.4e)

$$ {}_1F_3\left(l+1; l+\tfrac{3}{2}, \tfrac{l+B_{orb}+2}{2}, \tfrac{l-B_{orb}+2}{2}; \tfrac{-k^2}{16}\right)$$

is expressed using the infinite series representation of the generalized hypergeometric function to find

$$\frac{\Gamma\left(l+\frac{3}{2}\right)\Gamma\left(\frac{l+B_{orb}+2}{2}\right)\Gamma\left(\frac{l-B_{orb}+2}{2}\right)}{\Gamma(l+1)} \cdot \sum_{p=0}^{\infty} \frac{\Gamma(l+1+p)}{\Gamma\left(l+\frac{3}{2}+p\right)\Gamma\left(\frac{l+B_{orb}+2}{2}+p\right)\Gamma\left(\frac{l-B_{orb}+2}{2}+p\right)} \frac{\left(-\frac{k^2}{16}\right)^p}{p!}. \tag{5.18}$$

The first fraction of gamma functions is the reciprocal of Equation (5.4d) and so they will cancel one another.

5.2.3 The final form of $H_+(B_f)$

The results of the previous two subsections are combined to arrive at the representation of $H_+(B_f)$ that is applied in the matched filtering to follow. The g_1, g_2, g_3, g_4 and C functions are introduced to make the analysis more concise.

$$H_+(B_f) = \sum_{n=-\infty}^{\infty} \sum_{l=0}^{\infty} \sum_{m=-l}^{l} \sum_{p=0}^{\infty} \sum_{j=1}^{R} g_1 \cdot g_2 \cdot g_3 \cdot g_4 \tag{5.19a}$$

where the following definitions apply:

$$g_1 \equiv \frac{\sqrt{32}\pi^{\frac{5}{2}}}{\omega_r} \frac{k^{l+1/2}}{4^l} \left(\frac{-k^2}{16}\right)^p \frac{(l+p)!}{p!}$$

$$\cdot \frac{1}{\Gamma(l+p+3/2)} N_{lm}^2 P_l^{|m|}(\cos(\theta)) P_l^{|m|}(\cos(\alpha)) \tag{5.19b}$$

$$\cdot J_n\left(\frac{2\pi f_0 A \sin(\theta)}{c}\right)$$

$$g_2 \equiv \exp(iC) \tag{5.19c}$$

$$C \equiv \frac{\pi}{2}(l+n) - \frac{2\pi f_0 A \sin(\theta)\cos(\phi)}{c} - n\phi + m\phi + \pi(B_{mn} - l) \tag{5.19d}$$

$$g_3 \equiv \exp\left(i\pi(l - 2B_{mn})j\right) \tag{5.19e}$$

$$g_4 \equiv \frac{\exp(i\pi(1-2j)B_f)}{\Gamma\left(\frac{l}{2}+p+1+B_{mn}+B_f\right)\Gamma\left(\frac{l}{2}+p+1-B_{mn}-B_f\right)} \tag{5.19f}$$

The above functions are defined a manner such that:

1. g_1 is a real function not involving j or B_f.

2. g_2 is a complex function not involving j or B_f.

3. g_3 and g_4 are the only functions containing the j summation index.

4. g_4 is the only function containing the frequency term B_f.

Chapter 6

Derivation of the Inner Product

We now calculate the inner product using the definition given by Equation (4.14c). In order to differentiate between the signal and template expressions we denote the H's representing the signal as S's and let the H's denote the template. As discussed in section 4.3, we let the spectral noise density be a constant, that is, $S_n(f) \equiv M$ where M is some real number. The inner product expression $(H|S)$ to be evaluated is then

$$\int_{-\infty}^{\infty} \frac{2\Re\left(H^*(B_f)S(B_f)\right)}{M} df \tag{6.1a}$$

$$= \int_{-\infty}^{\infty} \frac{\Re\left((H_+^*(B_f) + H_+(-B_f))(S(B_f) + S^*(-B_f))\right)}{M} df \tag{6.1b}$$

$$= \frac{w_r}{2\pi M} \int_{-\infty}^{\infty} \Re\left[(H_+^*(B_f) + H_+(-B_f))(S(B_f) + S^*(-B_f))\right] dB_f \tag{6.1c}$$

$$\begin{aligned} = \frac{w_r}{2\pi M} \int_{-\infty}^{\infty} & \Re[H_+^*(B_f)S(B_f) + H_+(-B_f)S^*(-B_f) \\ & + H_+^*(B_f)S^*(-B_f) + H_+(-B_f)S(B_f)]dB_f \end{aligned} \tag{6.1d}$$

$$\equiv T_1 + T_2 + T_3 + T_4 \tag{6.1e}$$

The signal and template will both contain similar summation indices n, p, l, m, j and parameters θ, ϕ, f_0. In order to differentiate between them we use the convention that a bar over a symbol specifies that the symbol belongs to the signal, and a non-barred symbol belongs to the template. For example, $\bar{n}$ is a summation index for the signal, while n is a summation index for the template.

The integral over frequency is really only an integration over a g_4 and a $\bar{g}_4$ because the only parts containing B_f are contained in the respective g_4 subfunctions. We see for the previous expression that

$$T_1 \propto \int_{-\infty}^{\infty} g_4^*(B_f)\bar{g}_4(B_f)\ dB_f \tag{6.2}$$

$$T_2 \propto \int_{-\infty}^{\infty} g_4(-B_f)\bar{g}_4^*(-B_f)\ dB_f \tag{6.3}$$

$$T_3 \propto \int_{-\infty}^{\infty} g_4^*(B_f)\bar{g}_4^*(-B_f)\ dB_f \tag{6.4}$$

$$T_4 \propto \int_{-\infty}^{\infty} g_4(-B_f)\bar{g}_4(B_f)\ dB_f. \tag{6.5}$$

It turns out that the above integrals all share the common form

$$\int_{-\infty}^{\infty} \frac{e^{\imath 2\pi(\jmath-\bar{\jmath})B_f}}{\Gamma(c_1+B_f)\Gamma(c_2+B_f)\Gamma(d_1-B_f)\Gamma(d_2-B_f)}\ dB_f \tag{6.6}$$

where the $c_1,\ c_2,\ d_1,\ d_2$ definitions differ for each T:

	$\mathbf{c_1}$	$\mathbf{c_2}$	$\mathbf{d_1}$	$\mathbf{d_2}$
$\mathbf{T_1}$	a	$\bar{a}$	b	$\bar{b}$
$\mathbf{T_2}$	b	$\bar{b}$	a	$\bar{a}$
$\mathbf{T_3}$	a	$\bar{b}$	b	$\bar{a}$
$\mathbf{T_4}$	b	$\bar{a}$	a	$\bar{b}$

and where for convenience we introduce the following definitions: $a \equiv \frac{l}{2}+p+1+B_{mn}$, and $b \equiv \frac{l}{2}+p+1-B_{mn}$, which also follow the overhead bar notation. Integration of the common form involves two separate cases: $\jmath = \bar{\jmath}$ and otherwise. We begin with the latter.

6.0.4 Integral solution when $\jmath \neq \bar{\jmath}$

When $\jmath \neq \bar{\jmath}$ the integrals have the same form whose solution is given by [26]

$$\begin{aligned}&\int\limits_{-\infty}^{\infty} \frac{R(x)dx}{\Gamma[c_1+x, c_2+x, d_1-x, d_2-x]}\\&=\Gamma\left[\frac{c_1+c_2+d_1+d_2-3}{c_1+d_1-1, c_1+d_2-1, c_2+d_1-1, c_2+d_2-1}\right]\\&\cdot\int\limits_0^1 R(t)dt\end{aligned} \tag{6.7}$$

subject to the requirements $\Re(c_1+c_2+d_1+d_2) > 3$ and $R(x) = R(x+1)$. In all four cases we find $\Re(c_1+c_2+d_1+d_2) = l + 2p + \bar{l} + 2\bar{p} + 4 \geq 4$ and so the first requirement is met. For the second requirement, in all four cases, we find

$$R(B_f) \equiv e^{\imath 2\pi(\jmath-\bar{\jmath})B_f}. \tag{6.8}$$

We see that the second requirement is also met since

$$R(B_f+1) = e^{\imath 2\pi(\jmath-\bar{\jmath})(B_f+1)} = e^{\imath 2\pi(\jmath-\bar{\jmath})}R(B_f) = R(B_f). \tag{6.9}$$

The spectral noise density of GW detectors can be put into a partial fraction decomposition that allows for the use of Equation (6.9), which will be shown in a forthcoming publication. We find that the solution for each T is zero because

$$\int\limits_0^1 R(t)dt = \int\limits_0^1 e^{\imath 2\pi(\jmath-\bar{\jmath})t}dt = \frac{1}{\imath 2\pi(\jmath-\bar{\jmath})}\left(e^{\imath 2\pi(\jmath-\bar{\jmath})}-1\right) = 0. \tag{6.10}$$

6.0.5 Integral solution when $j = \bar{j}$

We now evaluate the remaining case. When $j = \bar{j}$ the exponential in the numerator of Equation (6.6) is equal to 1. The integrals then have the same form whose solution is given by [26]

$$\int_{-\infty}^{\infty} \frac{dx}{\Gamma[c_1 + x, c_2 + x, d_1 - x, d_2 - x]} = \Gamma\left[\frac{c_1 + c_2 + d_1 + d_2 - 3}{c_1 + d_1 - 1, c_1 + d_2 - 1, c_2 + d_1 - 1, c_2 + d_2 - 1}\right] \tag{6.11}$$

subject to the requirement that $\Re(c_1 + c_2 + d_1 + d_2) > 3$. The requirement is met, as it is identical to that for the $j \neq \bar{j}$ case already studied.

The following definitions are used to express the integral solutions concisely:

$$A \equiv \Gamma(a + \bar{b} - 1)\Gamma(b + \bar{a} - 1) \tag{6.12}$$

$$B \equiv \Gamma(a + \bar{a} - 1)\Gamma(b + \bar{b} - 1) \tag{6.13}$$

$$D \equiv \tfrac{(l+2p+\bar{l}+2\bar{p})!}{(l+2p)!(\bar{l}+2\bar{p})!} \tag{6.14}$$

The solution common to both the T_1 and T_2 integrals is $\frac{D}{A}$, while the solution common to both the T_3 and T_4 integrals is $\frac{D}{B}$.

6.0.6 Inner product expression snapshot

At this point the integration over frequency for the inner product is complete and we have the following expression for the inner product

$$\begin{aligned}(H|S) = {} & \sum_{n=-\infty}^{\infty}\sum_{l=0}^{\infty}\sum_{m=-l}^{l}\sum_{p=0}^{\infty}\sum_{\bar{n}=-\infty}^{\infty}\sum_{\bar{l}=0}^{\infty}\sum_{\bar{m}=-\bar{l}}^{\bar{l}}\sum_{\bar{p}=0}^{\infty}\sum_{j=1}^{R} \\ & \frac{w_r}{2\pi M} D g_1 \bar{g}_1 \left[\Re\left\{\frac{g_2^* g_3^* \bar{g}_2 \bar{g}_3}{A}\right\} + \Re\left\{\frac{g_2 g_3 \bar{g}_2^* \bar{g}_3^*}{A}\right\} \right. \\ & \left. + \Re\left\{\frac{g_2^* g_3^* \bar{g}_2^* \bar{g}_3^*}{B}\right\} + \Re\left\{\frac{g_2 g_3 \bar{g}_2 \bar{g}_3}{B}\right\} \right] \end{aligned} \tag{6.15a}$$

$$\begin{aligned} = {} & \sum_{n=-\infty}^{\infty}\sum_{l=0}^{\infty}\sum_{m=-l}^{l}\sum_{p=0}^{\infty}\sum_{\bar{n}=-\infty}^{\infty}\sum_{\bar{l}=0}^{\infty}\sum_{\bar{m}=-\bar{l}}^{\bar{l}}\sum_{\bar{p}=0}^{\infty}\sum_{j=1}^{R} \\ & \frac{w_r}{2\pi M} D g_1 \bar{g}_1 \left[\frac{2}{A} \Re\left(g_2 g_3 \bar{g}_2^* \bar{g}_3^*\right) + \frac{2}{B} \Re\left(g_2 g_3 \bar{g}_2 \bar{g}_3\right) \right] \end{aligned} \tag{6.15b}$$

6.0.7 Elimination of the summation over j

Before writing out the final inner product expression we note that it can be simplified further because the inner product is only non-zero when $j = \bar{j}$ and the sum over j can be solved by using the finite geometric series summation formula.

For the first summation over j of Equation (6.15b), we find

$$\sum_{j=1}^{R} g_3 \bar{g}_3^* = \sum_{j=1}^{R} e^{i\pi[(l-2B_{mn})-(\bar{l}-2\bar{B}_{mn})]j} = \sum_{j=1}^{R} x^j \tag{6.16}$$

where $x \equiv e^{i\pi[(l-2B_{mn})-(\bar{l}-2\bar{B}_{mn})]}$

$$= \begin{cases} \frac{x-x^{R+1}}{1-x} & \text{when } x \neq 1 \\ R & \text{otherwise.} \end{cases} \tag{6.17}$$

For the second summation over j of Equation (6.15b), we find

$$\sum_{j=1}^{R} g_3\bar{g}_3 = \sum_{j=1}^{R} e^{i\pi[(l-2B_{mn})+(\bar{l}-2\bar{B}_{mn})]j} = \sum_{j=1}^{R} x^j \tag{6.18}$$

where $x \equiv e^{i\pi[(l-2B_{mn})+(\bar{l}-2\bar{B}_{mn})]}$

$$= \begin{cases} \frac{x-x^{R+1}}{1-x} & \text{when } x \neq 1 \\ R & \text{otherwise.} \end{cases} \tag{6.19}$$

6.0.8 Final form of the inner product solution

The real part of a complex valued expression is required and to facilitate better notation we define the function G, which is used to express the real part of the two previous complex terms:

$$\mathrm{G}(w,x,y,z) \equiv \mathrm{S_R}(w,x)\cos(y+z) - \mathrm{S_I}(w,x)\sin(y+z) \tag{6.20}$$

$$\mathrm{S_R}(w,x) \equiv \begin{cases} \frac{s_1s_3-s_2s_4}{s_5} & \text{when } e^{i\pi(w+x)} \neq 1 \\ R & \text{otherwise} \end{cases} \tag{6.21}$$

$$\mathrm{S_I}(w,x) \equiv \begin{cases} \frac{s_1s_4+s_2s_3}{s_5} & \text{when } e^{i\pi(w+x)} \neq 1 \\ 0 & \text{otherwise} \end{cases} \tag{6.22}$$

where the symbols for S_R and S_I are defined as

$$s_1 \equiv \cos(\pi(w+x)) - \cos(\pi(w+x)(R+1)) \tag{6.23}$$

$$s_2 \equiv \sin(\pi(w+x)) - \sin(\pi(w+x)(R+1)) \tag{6.24}$$

$$s_3 \equiv 1 - \cos(\pi(w+x)) \tag{6.25}$$

$$s_4 \equiv \sin(\pi(w+x)) \tag{6.26}$$

$$s_5 \equiv 4\sin^2(\tfrac{\pi(w+x)}{2}) \tag{6.27}$$

We have derived the following exact closed-form solution for the inner product between a signal and a template:

$$\begin{aligned}(H|S) = &\sum_{p=0}^{\infty}\sum_{n=-\infty}^{\infty}\sum_{l=0}^{\infty}\sum_{m=-l}^{l}\sum_{\bar{p}=0}^{\infty}\sum_{\bar{n}=-\infty}^{\infty}\sum_{\bar{l}=0}^{\infty}\sum_{\bar{m}=-\bar{l}}^{\bar{l}} \\ &\cdot \frac{w_r}{\pi M} D g_1 \bar{g}_1 \Big[\tfrac{1}{A}\,\mathrm{G}(l-2B_{mn}, -(\bar{l}-2\bar{B}_{mn}), C, -\bar{C}) \\ &+ \tfrac{1}{B}\,\mathrm{G}(l-2B_{mn}, \bar{l}-2\bar{B}_{mn}, C, \bar{C})\Big].\end{aligned} \tag{6.28}$$

6.1 Bounds for the summands

An analytic bound for the summand of the inner product expressed by Equation (6.28) is now obtained. Upper bounds for the special functions and other factors of the summand will be given, and then their product will give rise to an upper bound for the total summand. The analytic bound can be used to obtain the rate of convergence of the inner product when the infinite series are truncated to obtain numerical results. This analysis is currently under study and not complete.

The g_1 function, Equation (5.19b), (and similarly for the barred version) present in the inner product solution has the following bounds for its factors:

$$\frac{(l+p)!}{\Gamma(l+p+\frac{3}{2})} < \frac{(l+p)!}{\Gamma(l+p+2)} \tag{6.29a}$$

$$= \frac{(l+p)!}{(l+p+1)!} \tag{6.29b}$$

$$= \frac{(l+p)!}{(l+p+1)(l+p)!} \tag{6.29c}$$

$$= \frac{1}{l+p+1}. \tag{6.29d}$$

The associated Legendre polynomials multiplied by a component factor of an N_{lm} with $1 \leq m \leq n$ has a bound [27]

$$\max_{x\in[-1,1]} |P_l^{|m|}(x)| \sqrt{\frac{(l-|m|)!}{(l+|m|)!}} < \frac{2^{5/4}}{\pi^{3/4}} \frac{1}{m^{1/4}}. \tag{6.30}$$

Using the above bound for the two associated Legendre functions we find

$$|N_{lm}|^2 |P_l^{|m|}(\cos(\theta))||P_l^{|m|}(\cos(\alpha))| < \frac{(2l+1)}{4\pi} \left(\frac{2^{5/4}}{\pi^{3/4}} \frac{1}{m^{1/4}} \right)^2 . \tag{6.31a}$$

The Bessel function has bounds given by [27]

$$|J_m(x)| \leq \begin{cases} \frac{2/\sqrt{\pi}}{[1+(\pi^4/16)x^4]^{1/16}} & \text{when } m \geq 1, \\ \frac{1}{[1+(\pi^4/16)x^4]^{1/8}} & \text{when } m = 0. \end{cases} \tag{6.32}$$

For the product of two gamma functions we find [28]

$$\Gamma(\tfrac{r}{2}+s+Q)\Gamma(\tfrac{r}{2}+s-Q)$$
$$= \left(\prod_{j=1}^{r} (r+s+d-j) \right) ((s-1)!)^2 \cdot \left(\frac{\pi d}{\sin(\pi d)} \right) \left(\prod_{m=1}^{s-1} \left(1 - \frac{d^2}{m^2} \right) \right), \tag{6.33}$$

with $s \equiv p + \bar{p} + 1$, $r \equiv l + \bar{l}$, $d \equiv Q - \frac{r}{2}$. When applied to A, $Q = B_{mn} + \bar{B}_{mn}$, and when applied to B, $Q = B_{mn} - \bar{B}_{mn}$.

For the factor D, recall that

$$D = \frac{(l+2p+\bar{l}+2\bar{p})!}{(l+2p)!(\bar{l}+2\bar{p})!}, \tag{6.34}$$

which is the reciprocal of the Beta function $B(l + 2p, l + 2\bar{p})$.

The remaining bound for the summand is for the function G. Looking at its definition we see that because G is a linear sum of two functions multiplied by the trigonometric functions sin and cos, its bounds will be determined by the bounds of $\mathrm{S_R}$ and $\mathrm{S_I}$. Although the previous functions involve the reciprocal of s_5, which can result in a value of 0 for certain combinations of w and x arguments, the functions $\mathrm{S_R}$ and $\mathrm{S_I}$ are in fact always finite due to cancelation of the denominator s_5, as can be checked by use of a few trigonometric identities. A more detailed analysis of the truncated series warrants careful study.

Chapter 7

Numerical Implementation

In this chapter, results from a numerical study of matched filtering using templates applied to a GW pulsar signal are given. To facilitate the study, a custom set of computer programs were written. The high performance *C++* [29] programming language is used for the programs that compute the fitting factor, Equation (4.15), values. Both serial and parallel program versions are written. The FF uses the analytically derived inner product expression of chapter 6, Equation (6.28). The *Matlab* [30] programming language is used primarily for the displaying of the numerical data obtained from the *C++* programs, and for minor data manipulations.

The writing of the programs is not an easy task because the analytic expression is difficult to compute using any naive numerical implementation. This aspect is discussed in section 7.3.

7.1 Computer hardware

The various results given in the following sections are dependent on the physical computer hardware that the programs run on. Specifically the speeds of the processors. For this thesis the hardware is provided by Shared Hierarchial Academic Research Computing Network (SHARCNET). SHARCNET is a multi-institutional high performance computer network that spans 17 leading academic institutions in Ontario, Canada [31]. Specifically, the computer cluster named Whale, see Figure 7.1, is used for most of the computations. Each node of the computer cluster consists of AMD

Opteron processors running at 2.2 GHz. The average memory used by the main fitting factor program is 4-7 MB. It is primarily the speed of the processors that determines the program runtimes, and not the speed of the memory used. This is found by running the program on systems with different processor speeds and memory, such as a laptop versus the SHARCNET cluster.

7.2 Computer libraries used

The *C++* computer programs are required to numerically compute the inner product expression, Equation (6.28), which contains the special functions of mathematical physics. The numerical implementation of any of the special functions is not a trivial exercise. The algorithms used are often quite complex and often found after extensive numerical analysis. For that reason an external computer library is used for the programs of this thesis, which is *The GNU Scientific Library* (GSL) [32]. It is a numerical library for C and C++ programmers that is provided for free under the *GNU General Public License* [33]. It provides numerical implementations of all of the special functions required. The version of the library used is 1.8.

7.3 Problems and solutions

The numerical implementation of the inner product given by Equation (6.28) is the most important algorithm written. This is because the fitting factor is the principal value desired when testing a template against a pulsar signal using matched filtering, and the FF is basically a ratio of three inner products. The efficient programming of the inner product is crucial to numerically performing matched filtering to measure a pulsar signal. The problems associated with programming the inner product are the following:

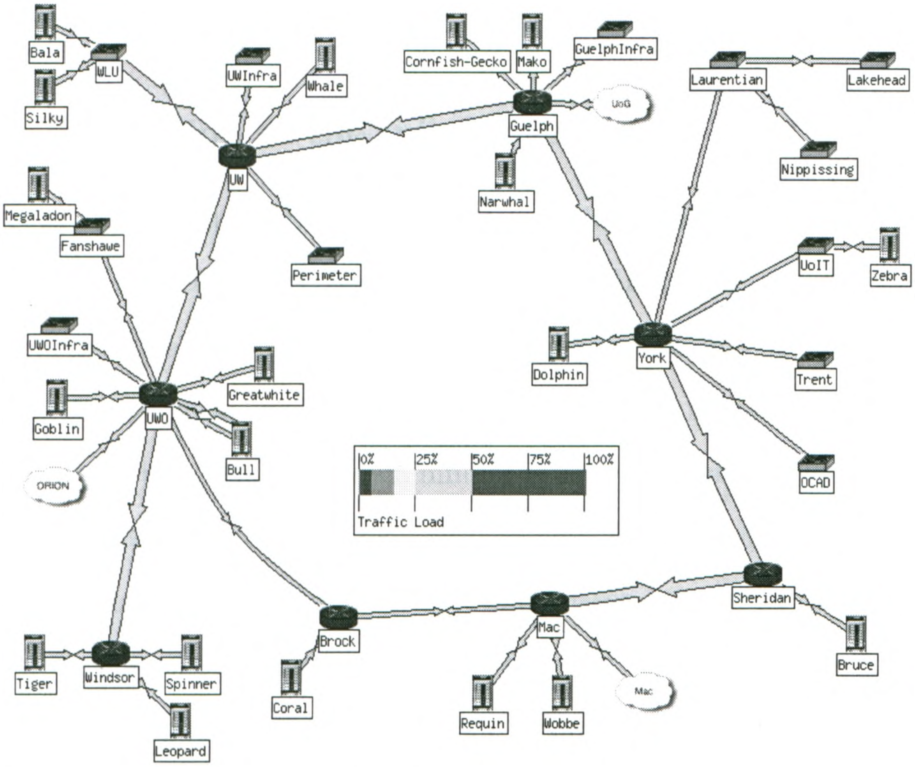

Figure 7.1: A network map of the available computer resources provided by Shared Hierarchial Academic Research Computing Network (SHARCNET) [31]. The main computer cluster used for this thesis is Whale. Other clusters used are Bruce, Dolphin, Greatwhite, Narwhal, Requin, and Silky. Source https://www.sharcnet.ca/cacti/plugins/weathermap/sharcnet.php

1. Truncation of the infinite series (see section 7.3.1)
2. Loss of precision (see section 7.3.2)
3. Underflows and overflows (see section 7.3.3)
4. Re-computation of time-costly summands (see section 7.3.4)

A summary of solutions to the problems is presented in section 7.3.5.

7.3.1 Truncation of the infinite series

The inner product solution, Equation (6.28), contains infinite series. This is a problem because computers cannot represent real numbers that have an infinite number of decimal places. The reason is that the numerical precision of a floating point number on a computer is finite, which means even an infinite series would effectively be truncated in practice. Therefore each infinite series was truncated to a variable index value. The number of terms required before the precision of the floating point number is reached is not easy to ascertain. For that reason, the inner product algorithm is written to take six integer arguments. Three of the integers are for the signal, and represent the maximum indices for the truncated summations over l, n, p. The remaining three integers are for the template, and represent the maximum indices for the truncated summations over $\bar{l}, \bar{n}, \bar{p}$. In symbols the following transformations are made

$$\sum_{l=0}^{\infty} \longrightarrow \sum_{l=0}^{L} \tag{7.1}$$

$$\sum_{n=-\infty}^{\infty} \longrightarrow \sum_{n=-N}^{N} \tag{7.2}$$

$$\sum_{p=0}^{\infty} \longrightarrow \sum_{p=0}^{P} \tag{7.3}$$

$$\sum_{\bar{l}=0}^{\infty} \longrightarrow \sum_{\bar{l}=0}^{\bar{L}} \tag{7.4}$$

$$\sum_{\bar{n}=-\infty}^{\infty} \longrightarrow \sum_{\bar{n}=-\bar{N}}^{\bar{N}} \tag{7.5}$$

$$\sum_{\bar{p}=0}^{\infty} \longrightarrow \sum_{\bar{p}=0}^{\bar{P}} \tag{7.6}$$

Using the L, N, P, $\bar{L}$, $\bar{N}$, and $\bar{P}$ arguments allows for the truncation of the infinite series to arbitrary indices. The specific values that those integers take has a dramatic effect on the computation time of the inner product. A study of the integer arguments effects on program performance is studied in section 8.1.

7.3.2 Loss of precision

A difficult problem to solve is the loss in precision of the summands. Unlike in algebraic mathematics, the expression $(ab)/c$ is not always equivalent to $a(b/c)$ when computed numerically. This is due to the floating point arithmetic IEEE standard that most computers use. Also, division by a large number or subtraction of equivalent numbers can result in a great loss in precision of the floating point numbers. For this reason, the order in which the functions of the summand should be computed has to be determined. This is done by beginning with some basic facts and then using numerical observations of the stabilities of the various possibilities of the order of operations. The goal is the minimization of the loss of precision. This problem is also related to the large numbers resulting from the factorials and gamma functions, as well as the alternating signs of the summands.

A straight numerical implementation of the G function, Equation (6.20), does not work, as it is numerically unstable when its values are studied through various test runs of the program. For this reason, an algebraically equivalent algorithm is used. The function G was principally defined for use in the algebraic derivation of the inner product in chapter 6, and the study of the bounds of the summand.

7.3.3 Underflows and overflows

The many factorials and gamma functions result in extremely large magnitude values. The multiplication and division of such extreme values can result in underflows and overflows, which can crash the computer program. A partial solution is to take the logarithm of the summand of Equation (6.28). This replaces the multiplications and divisions of the larger numbers, with additions and subtractions of smaller numbers. It then takes a much larger value to crash the computer, but such values do occur. The result is that underflows and overflows are less common, and so the program runs for a longer time before crashing. That is, the only difference is that the summation indices need to be larger before underflows and overflows reappear.

The underflow errors are not as difficult to prevent as the overflow errors. The solution used is to detect that an underflow is about to happen, and then to set the value in question to zero. This is justified because adding a number smaller than the smallest machine number representation does nothing to a floating point number.

A greater problem is the occurrence of many overflow errors. The magnitudes that occur when computing a summand are so large that it overflows the floating point numbers used to store them in. The first solution to this problem is to use a large number library that has an equivalent floating point representation but that can contain immensely larger values. This stops the overflows. The library used is the *GNU Multiple Precision Arithmetic Library* [34], which is a free large number library distributed on the internet. The drawback with using such a library is that the computation times necessarily increase due to the extra bookkeeping and computation needed to manage the larger numbers. This has a huge effect on the computation time of the program because of the large number of summands being summed. Anything that effects the computation time of the summands, even a seemingly innocuous addition operation, has profound effects. The programs that are run with this library are too inefficient, so an alternative solution has been formulated.

By analyzing the values of the summands for long sequences it is seen that the final values for the inner product are well within the range provided by the floating point numbers of the SHARCNET machine. That is, using the large number library results in final values for the inner products that are of the order 10^{40} (see Table 8.1), which is well within the range of the floating point numbers used. This is another indicator that the problem lies in the sequences of summands. It is only the fact that, seemingly randomly, a long sequence of additions occurs that can result in an overflow. That is, though there are large negative summands to offset the large positive ones, if they do not occur at around the same time an overflow happens. So, a second solution, which is the one used for the rest of this thesis, is to use the sorted *Kahan Summation algorithm* [35] on blocks of summands. By *block* is meant a set number of sequential summands.

The Kahan summation algorithm in pseudo-code is the following [36]

```
function kahanSum(input, n)
 var sum = input[1]
 var c = 0.0
 for i = 2 to n
```

```
    y = input[i] - c
    t = sum + y
    c = (t - sum) - y
    sum = t
  next i
return sum.
```

It adds numbers, taking into account the precision and roundoff error of the machine floating point representation. This results in more decimal places of accuracy. It is worth looking at the last steps of the algorithm in regards to floating points arithmetic. When $t = sum + y$ is substituted into $c = (t - sum) - y$, the result is $c = ((sum + y) - sum) - y = 0$. Therefore, using analytic mathematics c is being set to zero, but this is not the case numerically. In fact, c is being set to a small value. This is an instance of when the order of numerical operations matters and floating point arithmetic greatly affects a computation, as is discussed about in section 7.3.3.

In the program implementation, a block of summands is the input to the Kahan algorithm, and their sum is the output. The output is is added to the running total for the inner product. The result is that the long sequences are broken apart and the positives and negatives are taken in approximately equal numbers to offset each other, which eliminates the overflow errors. In addition to eliminating the overflows, the value of an inner product is also more accurate, having less precision loss due to the use of the Kahan algorithm.

7.3.4 Re-computation of time-costly summands

The most straight-forward numerical implementation of Equation (6.28) is to use 8 nested loops representing the 8 summations. This results in a large number of computations that are continually, and needlessly, repeated. The reason is that there are only a few products of the inner product summand that are functions of the indices from both the signal and the template simultaneously. The summands are already computationally intensive due to the large number of special functions involved. Computing J_n because the value of $\bar{n}$ changed is not efficient. A more efficient manner is to compute values once and store them in two *caches.* A cache is a fixed set of memory that is designed to store a set of numbers, and is to be accessed frequently. The program implementation uses two caches. One is for the signal and one is for the template. The sizes of the caches are

$$(L+1)^2(2N+1)(P+1) \quad \text{for the signal,} \tag{7.7}$$

$$(\bar{L}+1)^2(2\bar{N}+1)(\bar{P}+1) \quad \text{for the template.} \tag{7.8}$$

The formula for the size of the signal cache is determined as follows (similarly for the template cache):

$$\sum_{p=0}^{P} \text{ has } P+1 \text{ terms} \tag{7.9}$$

$$\sum_{n=-N}^{N} \text{ has } 2N+1 \text{ terms} \tag{7.10}$$

$$\sum_{l=0}^{L} \text{ and } \sum_{m=-L}^{L} \quad \text{has } \sum_{l=0}^{\infty}(2l+1) \text{ terms.} \tag{7.11}$$

For the last two summations it is seen that

$$\sum_{l=0}^{\infty}(2l+1) = \sum_{l=0}^{L} 2l + \sum_{l=0}^{L} 1 \tag{7.12}$$

$$= 2\left(\frac{L(L+1)}{2}\right) + L \tag{7.13}$$

$$= L(L+1) + L \tag{7.14}$$

$$= (L+1)^2 \text{ terms.} \tag{7.15}$$

The caches are precalculated before being used in the main algorithm. The values of the signal cache represent the summand sequence of

$$\sum_{p=0}^{\infty}\sum_{n=-\infty}^{\infty}\sum_{l=0}^{\infty}\sum_{m=-l}^{l} g_1. \tag{7.16}$$

The values of the template cache represent the summand sequence of

$$\sum_{\bar{p}=0}^{\infty}\sum_{\bar{n}=-\infty}^{\infty}\sum_{\bar{l}=0}^{\infty}\sum_{\bar{m}=-\bar{l}}^{\bar{l}} \bar{g}_1. \tag{7.17}$$

Pseudo-code for the method is the following

```
1. Calculate the cache for the signal.
2. Calculate the cache for the template.
3. For the innermost of the 8 nested loops,
   use values from the two caches, and
   calculate the values that require indices
   from both the signal and template simultaneously.
```

Using the two caches one entire set of caches does not have to be continually recalculated when an index changes in one of the outermost loops. This has a dramatic effect on the computation times, allowing them to be completed in reasonable times that range from seconds to hours (see Table 8.1 for specific runtimes).

7.3.5 Summary of solutions

The infinite series are truncated to arbitrary index values, L, N, P, $\bar{L}$, $\bar{N}$, and $\bar{P}$. The values are provided as arguments to the inner product algorithm. The underflows are caught before causing an error, and set to a value of 0. The overflows are handled by adding blocks of summands using the Kahan summation algorithm, which has the additional benefit of reducing the precision loss in the numbers. The re-computation of time-consuming summands is taken care of by using two caches. The eight nested loops then, for the most part, look up summands from the two caches. The remaining computations to determine a summand are for functions that use both the signal and template indices simultaneously (*which is why they cannot be cached*). These solutions result in an efficient numerical algorithm and program for the inner product solution.

Chapter 8

Numerical Studies

This chapter presents the results of numerical studies that use the numerical implementation described in chapter 7. The bounds for the summand of Equation (6.28), which indicates how fast the series converges, is given in section 6.1. The numerical runtimes, values, and associated error bounds are given in section 8.1. A pulsar model parameter space study is performed in section 8.2. Lastly, statistics of the threshold crossings are ascertained in section 8.4. The threshold crossing statistics is indicative of how well the method works in practice at detecting a pulsar signal.

8.1 Effects of the truncated indices

The program used to calculate the fitting factors truncates the infinite series to indices given by L, N, P, $\bar{L}$, $\bar{N}$, and $\bar{P}$, as explained in section 7.3.1. Their relationship to the computation times, the fitting factor values, and their associated absolute error bounds are studied in this section. To provide for a more uniform study, all of the indices were given the same value, which would be any positive integer. The value is termed the *uniform index.* For example, if the unform index is 5, then $L = N = P = \bar{L} = \bar{N} = \bar{P} = 5$. Numerical results for various uniform index values are given in Table 8.1.

Table 8.1: Inner product uniform index statistics

Uniform Index, U	**Inner Product Value**	**Absolute Error**	**Total Time (s)**	**Computation Time (s)**
0	5.83E-007	2.35E-020	0	0.09
1	23652.2	6.95E-009	0	0.1
2	8.93E+011	754.82	0	0.25
3	3.49E+017	6.44E+008	4	1.91
4	1.09E+022	3.67E+013	22	11.53
5	7.32E+025	4.88E+017	111	51.91
6	2.37E+029	2.16E+021	556	185.65
7	1.46E+032	2.39E+024	1653	552.58
8	2.37E+034	8.63E+026	3854	1430.58
9	9.82E+035	1.09E+029	4946	3393.31
10	1.55E+037	6.13E+030	8868	7307.61
11	1.04E+038	1.64E+032	36850	14910.2
12	4.79E+038	2.54E+033	71041	28522.4
13	1.28E+039	2.99E+034	96582	51724.71
14	1.93E+039	3.93E+035	135465	89956.77
15	1.36E+039	5.34E+036	162827	150267.95
16	5.38E+038	7.17E+037	277163	246823.17
17	1.17E+038	8.98E+038	416720	388664.69
18	1.77E+037	1.01E+040	631410	603261.19

8.1.1 Inner product runtimes

The most striking property of Table 8.1 is the dramatic increase in computation time for an increase in the uniform index. The evaluation times are plotted in Figure 8.1. There are two series plotted because there are two times reported. One time is the *computation time*, which is actually used for computation by the program. The second longer time is the *total time*, which is the time it takes to run the program on SHARCNET and obtained results. The total time is important since it is what actually elapses before an output is obtained. It is most likely highly dependent on the configuration of the SHARCNET cluster. For this reason the computation time is focused on.

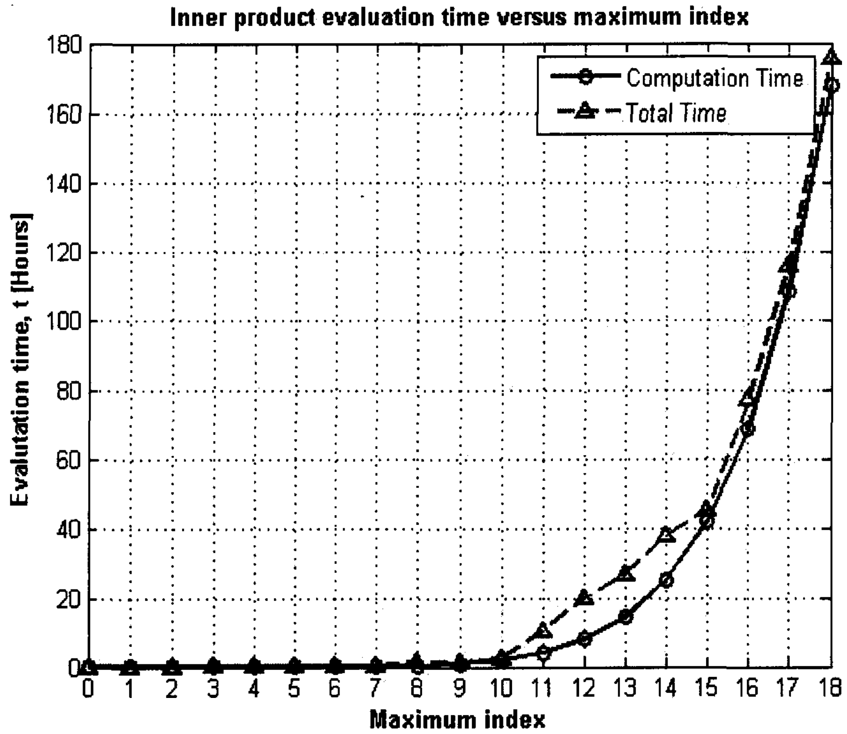

Figure 8.1: Inner product runtimes.

An exponential increase with uniform index value is the general pattern. This is understandable because of the eight nested summations and total number of summands. Even though two caches are being used, they still need to be computed.

Also, the single increases in each index are multiplied together. The total number of summands is given by

$$(P+1)(2N+1)(L+1)^2(\bar{P}+1)(2\bar{N}+1)(\bar{L}+1)^2. \tag{8.1}$$

In terms of the uniform index, denoted U, the total number of summands, denoted V, is given by

$$\begin{aligned} V &= (U+1)(2U+1)(U+1)^2(U+1)(2U+1)(U+1)^2 && (8.2) \\ &= (U+1)^6(2U+1)^2. && (8.3) \end{aligned}$$

The average time per individual summands is found by dividing the times given in Table 8.1 by the total number of summands as given by Equation (8.2). The average times is $m = 2.670410^{-9}$ seconds per summand. A plot of mV versus uniform index is shown in Figure 8.2. The theoretical prediction, mV, for the computation time matches the actual computation time almost perfectly. Equation (8.2) can be used to predict the runtimes for any uniform index. The results indicate that each summand of an inner product is taking approximately the same time to compute.

8.1.2 Inner product values and errors

Each of the special functions supplied by the GNU GSL programming library provides a maximum possible absolute error estimate for one use of the function. The absolute errors depend upon the parameters used with for each special function. When multiplying special functions the maximum absolute errors were also taken into account by the fitting factor program. The inner product algorithm would return a value for the inner product as well as a maximum absolute error for that value. These absolute errors are not the difference between the untruncated inner product expression and

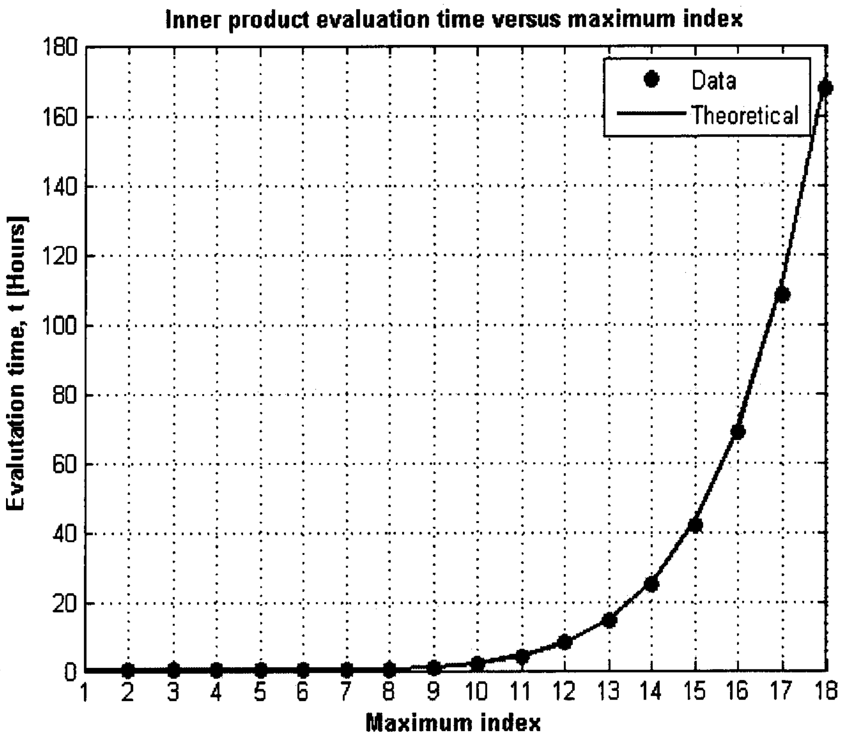

Figure 8.2: Theoretical performance times.

the truncated one used numerically.

The dramatic increase in the absolute error of the values is of concern. As can be seen, the values are unusable at around a uniform index in the range 16 to 17. At least based on the implementation used, going to higher uniform indices is not useful due to the fact that none of the values will be precise. This is a concern because it is desirable to compute the inner product for larger indices so as to further test the behavior of the inner product solution. An asymptotic analysis warrants careful study.

8.2 Pulsar parameter space studies

The program numerically calculated the fitting factors, using the inner products given by Equation (6.28) with Equation (4.15), for various signal and template parameters,

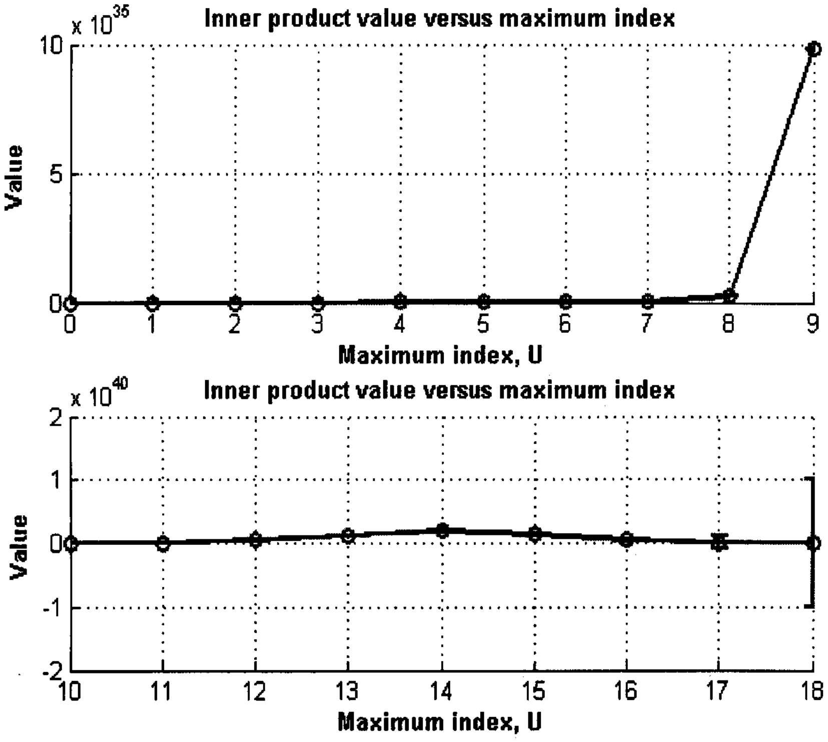

Figure 8.3: Inner product values.

which we now present. It should be noted that the values of the signal and template parameters themselves, the angles and frequency, do not affect the computation times.

8.2.1 Full parameter plot

In order to study the relationship between the source angles ϕ and θ, and those angles parameterizing a template, we fixed $\alpha = 90$ degrees and $f_0 = 800.01$ Hz for both the pulsar GW signal and the templates. In Figure 8.4 we show the results of a study over a fine mesh in the template ϕ and θ parameter domain. Templates parameterized by differing θ and ϕ were generated and totalled in number at 4225. The total computation time equivalent to a single processor was 329070 seconds. The resolution of the angle mesh is not for every degree, however it is detailed enough *to show a definite pattern. There are two main structures. They look like parallel mountain ranges in the* θ_T *direction. One of them is with* $\phi_T = 72$ *degrees, which is*

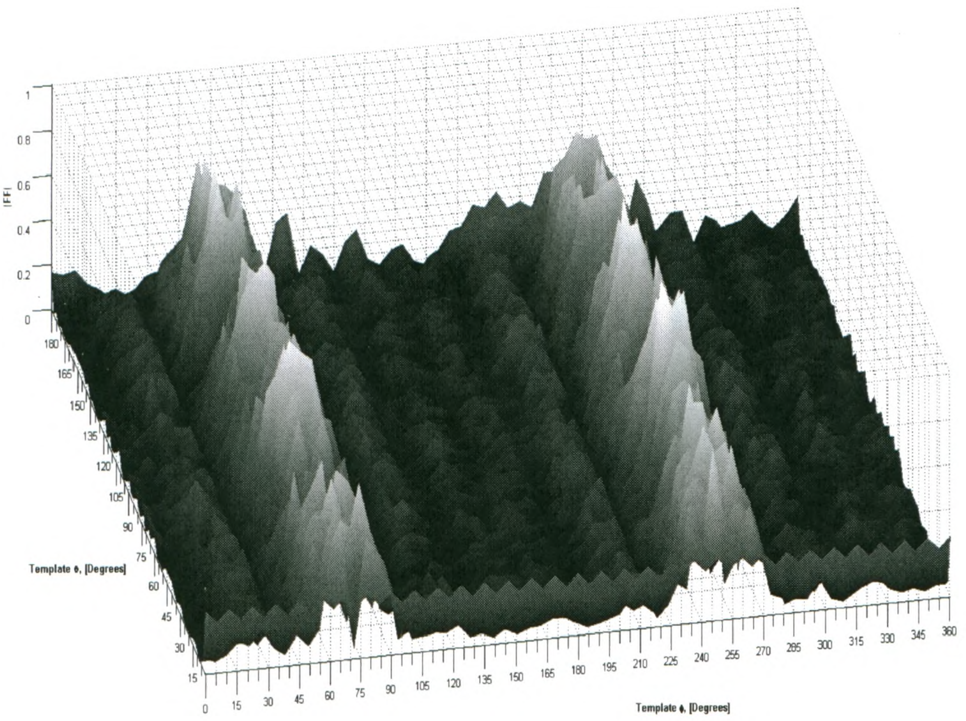

Figure 8.4: The FF versus ϕ and θ for a signal with $\{\alpha, \phi, \theta, f_0\}_{signal} = \{90, 72, 69, 800.01\}$ and with templates with $\{\alpha, \phi, \theta, f_0\}_{template} = \{90, varied, varied, 800.01\}$. The infinite summation indexes were truncated at $L = N = P = \bar{L} = \bar{N} = \bar{P} = 6$. The 4225 fitting factors were calculated in 329070 seconds.

the same as the signal itself, and the other is at $\phi_T + 180 = 252$ degrees. Between the two main structures the fitting factor values are quite low, and the pattern is that of smaller mountain ranges in the same direction as the two main ones. There appears to be a definite relationship between $\phi_T = \phi_S$ and $\phi_T = \phi_S + 180$ degrees. Having seen the larger structure of the parameter space, we now look at finer plots of the ranges and their cross sections.

8.2.2 Azimuthal plot for $\theta_T = \theta_S$

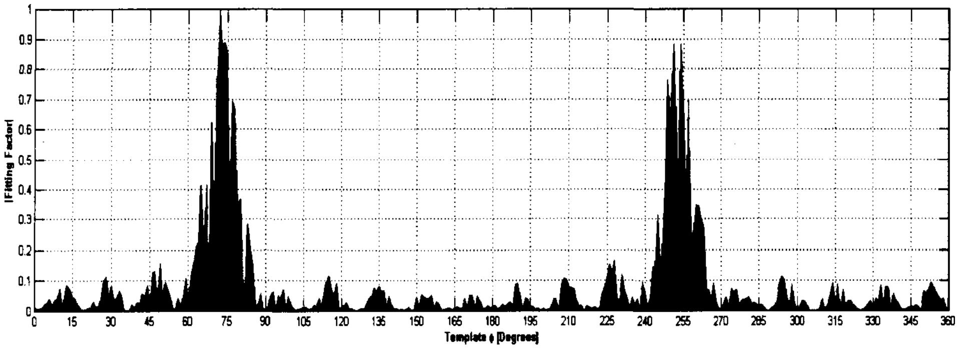

Figure 8.5: The FF versus ϕ_T for $\{\alpha, \phi, \theta, f_0\}_{signal} = \{90, 72, 69, 800.01\}$ and $\{\alpha, \phi, \theta, f_0\}_{template} = \{90, varied, 69, 800.01\}$. The summation indexes were truncated to $L = N = P = \bar{L} = \bar{N} = \bar{P} = 10$ and the runtime was 4330576 seconds.

To study the variation of fitting factor with template ϕ, we fixed θ of the templates to be equal to that of the GW signal, which was $\theta_S = 69$ degrees. The templates differed in ϕ by 1 degree, with all other values being identical, and were found for the entire ϕ_T interval. The 360 fitting factors were calculated in an equivalent single processor time of 4330576 seconds, with the summation indexes truncated to 10. The resulting values were plotted and are shown in Figure 8.5.

The largest FF has a value of 1 and occurs at template $\phi = 72$ degrees, which is a perfect match for the GW signal. The figure shows a striking change in FF value over a single degree change in ϕ_T. This can be accounted for by the many periodic special functions of mathematical physics and the trigonometric functions that are part of the inner product solution. As noted in an earlier section, a FF lower limit of ≈ 0.9 will signify that a template's parameters are close to that of the signal. For the present case there would only be 2 candidate parameter sets, and we know that one of them matches the actual signals. The second large peak at $\phi_T = 252$ degrees belongs to the second mountain range of Figure 8.4.

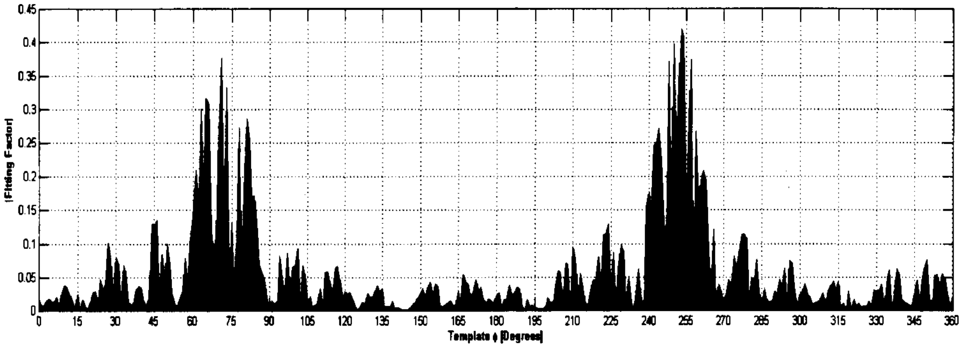

Figure 8.6: The FF versus ϕ_T for $\{\alpha, \phi, \theta, f_0\}_{signal} = \{90, 72, 69, 800.01\}$ and $\{\alpha, \phi, \theta, f_0\}_{template} = \{90, varied, 159, 800.01\}$. The summation indexes were truncated to $L = N = P = \bar{L} = \bar{N} = \bar{P} = 10$ and the runtime was 4266016 seconds.

8.2.3 Azimuthal plot for $\theta_T = \theta_S + 90$ degrees

To see in detail what happens if the template θ does not match that of the GW signal, we show Figure 8.6. The signal parameters were the same as for Figure 8.5, but this time θ of the templates was $\theta_T = \theta_S + 90 = 159$ degrees, and so 90 degrees larger than that of the signal. The FF was again calculated for each template, where the templates differed only in ϕ, and ranged from 0 to 360 degrees. The resulting figure does not show any FF values above ≈ 0.41. Using the criterion of a $FF > 0.9$ to signify a good match, none of the templates observed at $\theta_T = 159$ are close to matching. Having looked at the variation of the FF with ϕ_T in detail, we now look at the variation in FF with θ_T by observing the two mountain ranges up close.

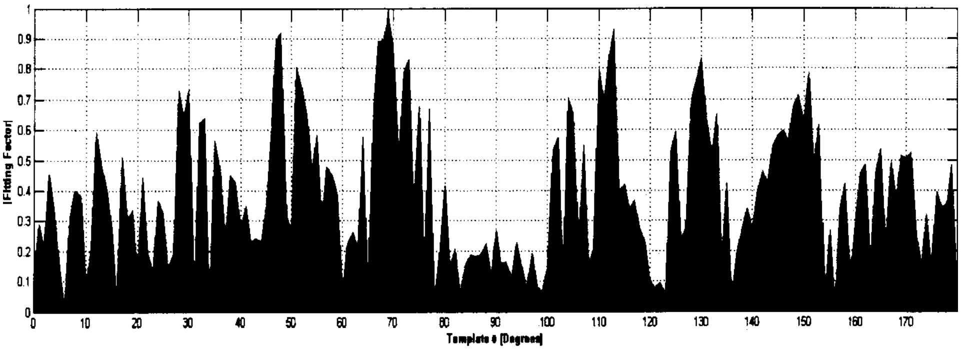

Figure 8.7: The FF versus θ_T for $\{\alpha, \phi, \theta, f_0\}_{signal} = \{90, 72, 69, 800.01\}$ and $\{\alpha, \phi, \theta, f_0\}_{template} = \{90, 72, varied, 800.01\}$. The summation indexes were truncated to $L = N = P = \bar{L} = \bar{N} = \bar{P} = 10$ and the runtime was 2159315 seconds.

8.2.4 Colatitude plot for $\phi_T = \phi_S$

Using the same signal as before, and with $f_T = f_S$ and $\phi_T = \phi_S$, we observe the mountain range containing the signal parameters up close by plotting FF versus θ_T, which is shown in Figure 8.7. The maximum FF, and greatest match, is at $\theta_T = \theta_S = 69$ degrees, as expected. However, there are also two other peaks greater than the 0.9 threshold. Combining knowledge of the FF from the varying ϕ plot, the greatest match for both angles is at the actual signal angles. A high degree of symmetry is also seen in the plot, which we are currently working to explain analytically.

8.2.5 Colatitude plot for $\phi_T = \phi_S + 180$ degrees

Looking at the second mountain range at $\phi_T = \phi_S + 180 = 252$ degrees, shown in Figure 8.8, we see the same general shape as for the the first mountain range, however the maximum peak is lower than before and there are now only two peaks that are at 0.9 or greater. Interestingly, one of them is at $\theta_T = 72$ degrees, and the other at $\theta_T = 110$ degrees.

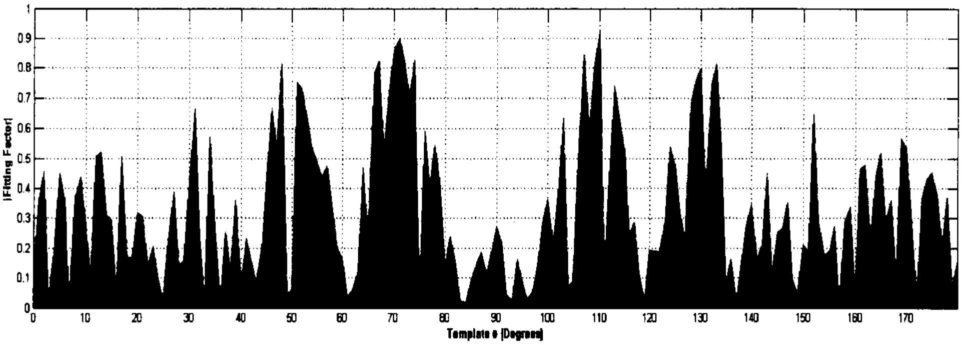

Figure 8.8: The FF versus θ_T for $\{\alpha, \phi, \theta, f_0\}_{signal} = \{90, 72, 69, 800.01\}$ and $\{\alpha, \phi, \theta, f_0\}_{template} = \{90, 252, varied, 800.01\}$. The summation indexes were truncated to $L = N = P = \bar{L} = \bar{N} = \bar{P} = 10$ and the runtime was 2145032 seconds.

8.3 Frequency study

The relationship between the frequency of the signal and the frequency of the template is studied in this section. For all of the results of this section the parameters were $\alpha = 90$ degrees, $U = 6$, $\phi_T = \phi_S = 72$ degrees, and $\theta_T = \theta_S = 69$ degrees. The only parameter that is different between the signal and templates is the frequency. The signal itself is at 800.01 Hz.

Shown in Figure 8.9 in a broad frequency plot of the FF from 1 Hz to a little over 800 Hz. The plot immediately seems odd because there is not a peak around the signal frequency, as would intuitively be expected. Also, the magnitudes are all extremely small. Even the largest values shown are essentially zero and can be attributed to floating point errors. A second plot which looks at a narrow frequency range centered around the signal frequency is next shown in Figure 8.10, and an even narrower band in Figure 8.11.

In the last two figures mentioned a peak is shown, consisting of a value of 1.0, and all others are essentially zero. This gives the odd impression of a delta function. Also, in studies of this it was observed that unless the template frequency matches exactly that of the signal, there will not be any peak at all! This is quite an odd behavior, and I am attempting to explain it analytically. I believe it has to do with the G function, Equation (6.20). Whatever the cause, it shows that the matched filtering solution is extremely discriminatory for the frequency parameter, which has both a pro and a con. The pro is that if a peak is found, we essentially know the true signal frequency, while the con is that finding the value would be extremely time consuming and search intensive.

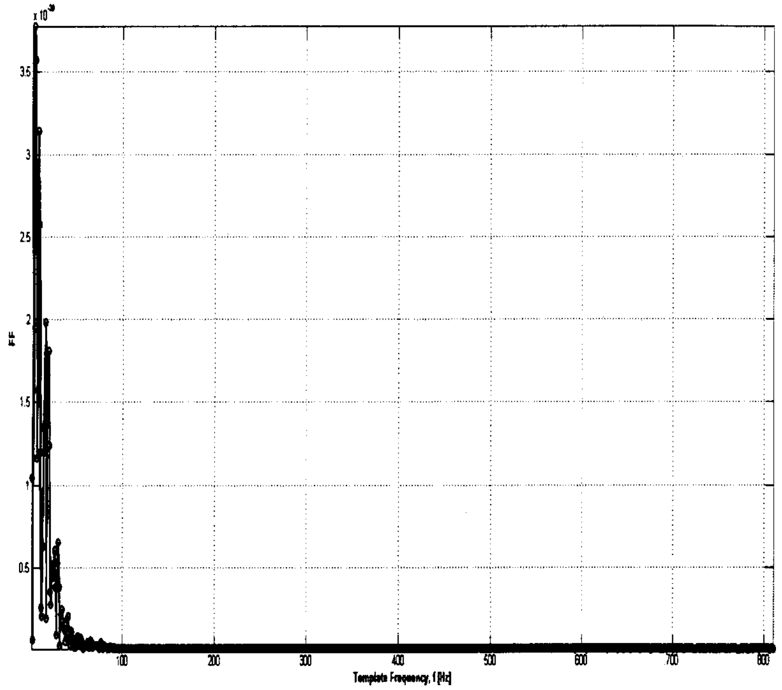

Figure 8.9: Variation of template frequency. $f_T = 1$ to 810 Hz where $\Delta f = 1$ Hz.

8.4 Threshold crossings

A threshold is a given FF value. A threshold crossing is any FF value that is greater than a given threshold. In order to obtain statistics on the threshold crossings, 29 regular lattice meshes were created and evaluated. One signal was used per mesh, and its parameters were chosen randomly. The frequency of the templates was set equal to that of the signal. The 29 meshes were used to determine the number of

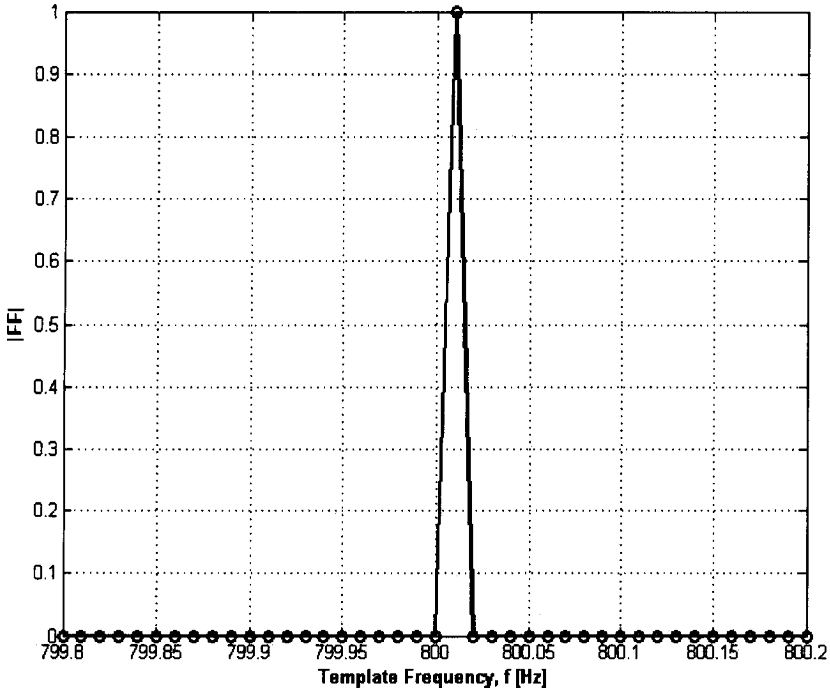

Figure 8.10: Variation of template frequency. $f_T = 799.8$ to 800.2 Hz where $\Delta f = 0.01$ Hz.

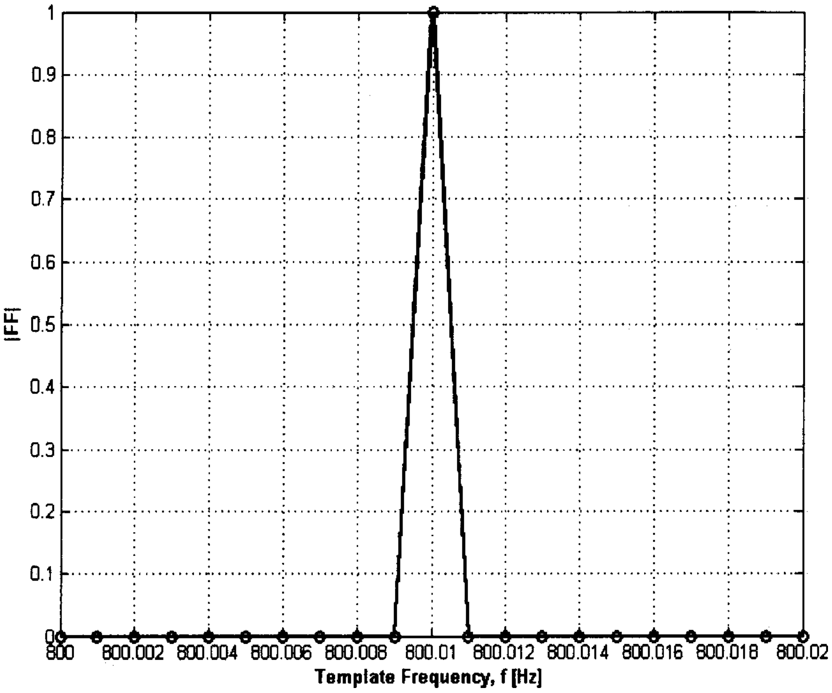

Figure 8.11: Variation of template frequency. f_T = 800 to 800.02 Hz where $\Delta f = 0.001$ Hz.

threshold crossings, and also to ascertain the probability that a template associated with a given FF value will be within a 15 degree radius of the signal.

8.4.1 Threshold crossings for a single mesh

The threshold crossings for a single mesh are given in Figure 8.12. A zoomed-in version of the threshold is shown in Figure 8.13.

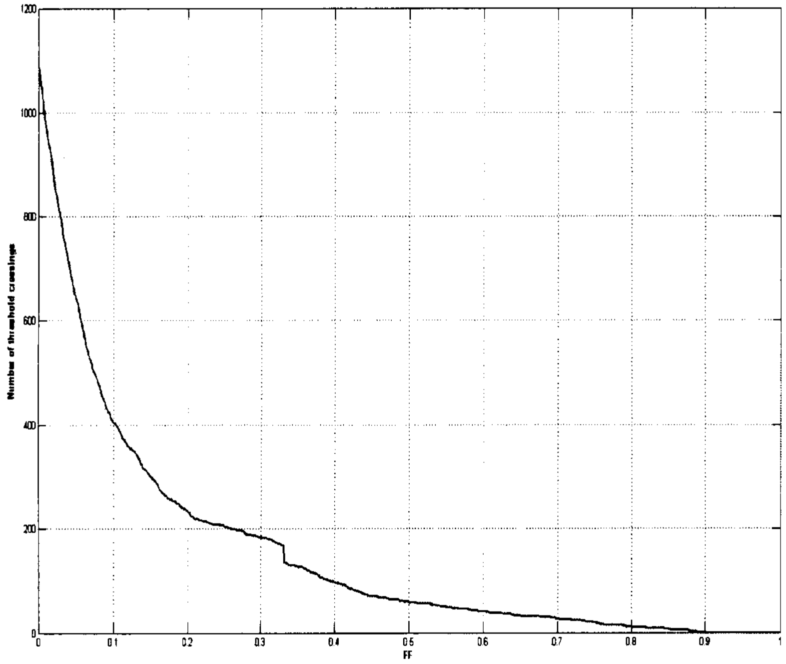

Figure 8.12: Threshold crossings

8.4.2 Total number of threshold crossings for 29 meshes

The threshold crossings totals for 29 meshes are shown in Figures 8.14.

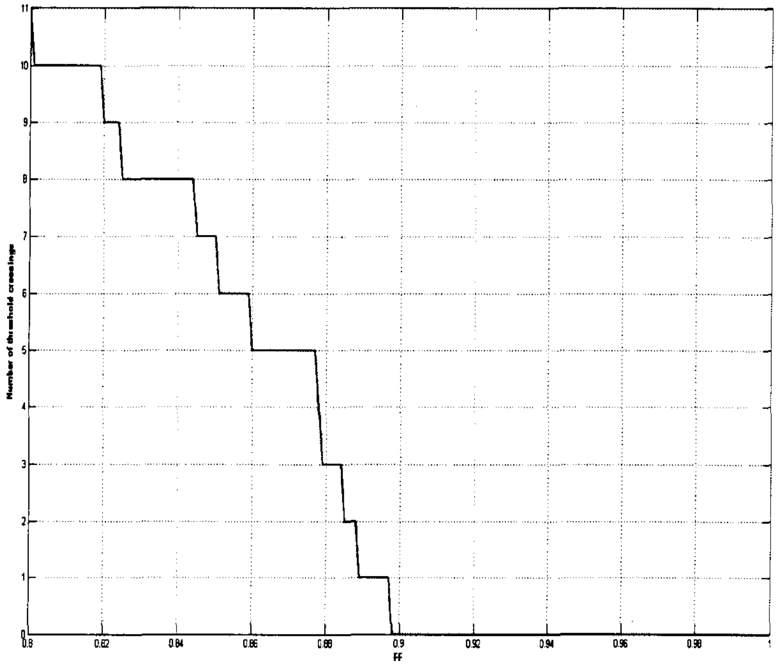

Figure 8.13: Threshold crossings zoomed

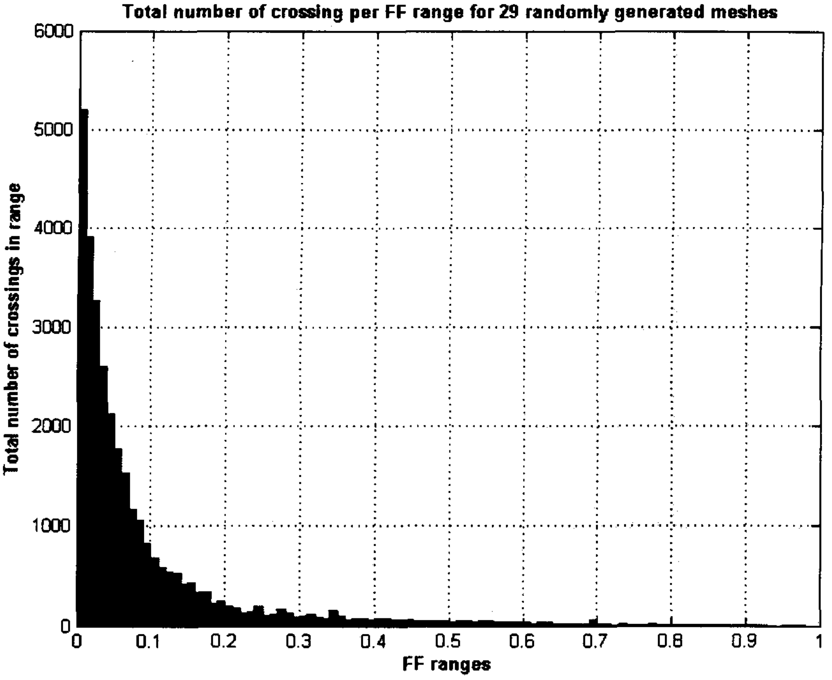

Figure 8.14: The total number of threshold crossings per FF value. A total of 29 meshes, each for stage 6, were used.

8.4.3 Probability of matching

Given the FF value of a template, how likely are the templates parameters to be within a given radius, in the (θ, ϕ) space, of a signal? That is the question that is answered in this section. To do so a custom procedure is used. For a given FF value, the probability is defined to be the total number of templates having the given FF value and being within the radius of the signal, divided by the total number of templates having the given FF. The fraction has values between 0 and 1. This procedure is performed for 29 meshes and the results of the total averaged. Figure 8.15 presents the resulting probabilities. It allows for false positive and false negatives of measurement to be determined for various thresholds. Some of the individual meshes used in the analysis are shown in Figures 8.16, 8.17, 8.18, 8.19, 8.20, and 8.21. In the plots, the thicker line is located at the signal parameters, and the narrower lines represent the templates that are within the given radius of the signal. The results indicate that a $FF > 0.9$ will have more than a 50 percent chance of lying within a 15 degree radius of a signal.

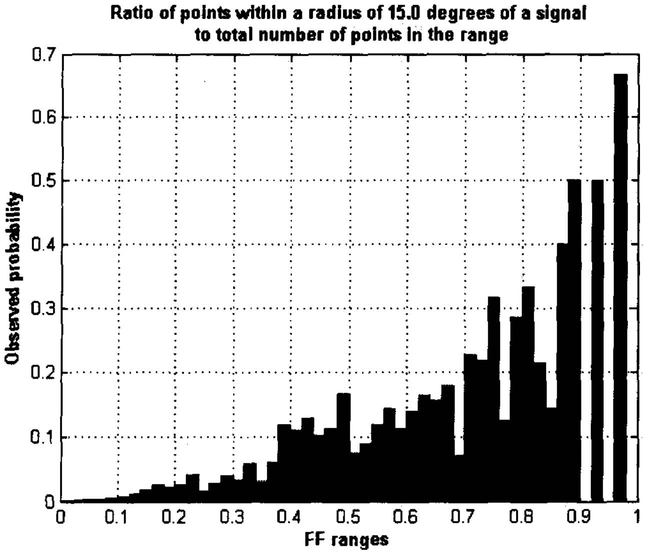

Figure 8.15: The probability that a template is within a 15 degree radius of the signal when above a threshold value. A total of 29 meshes, each for stage 6 (1089 point), were used.

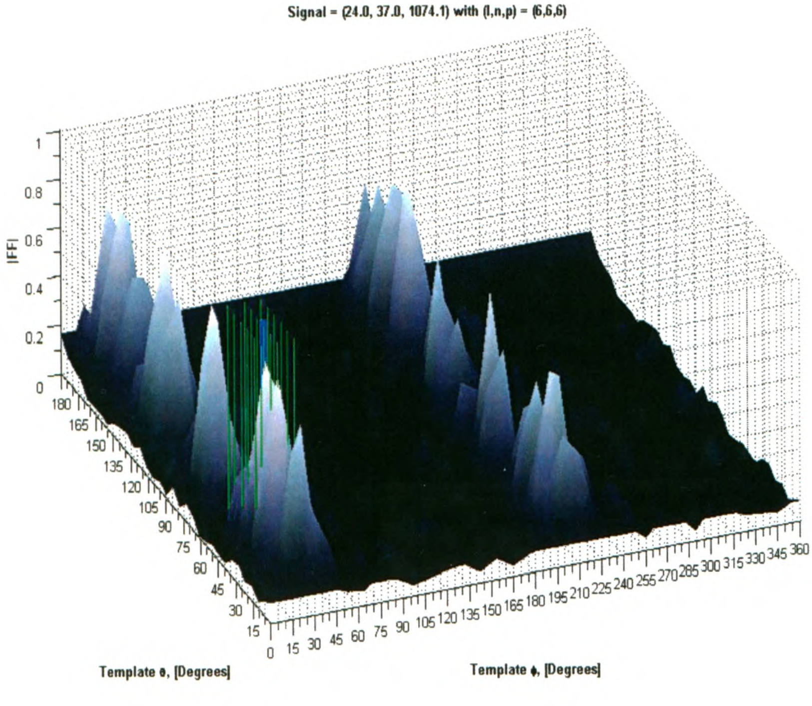

Figure 8.16: A parameter mesh used, which contained 1089 points. The thick vertical line represents the source location. The smaller vertical lines represent templates that were within a 15 degree radius of the signal.

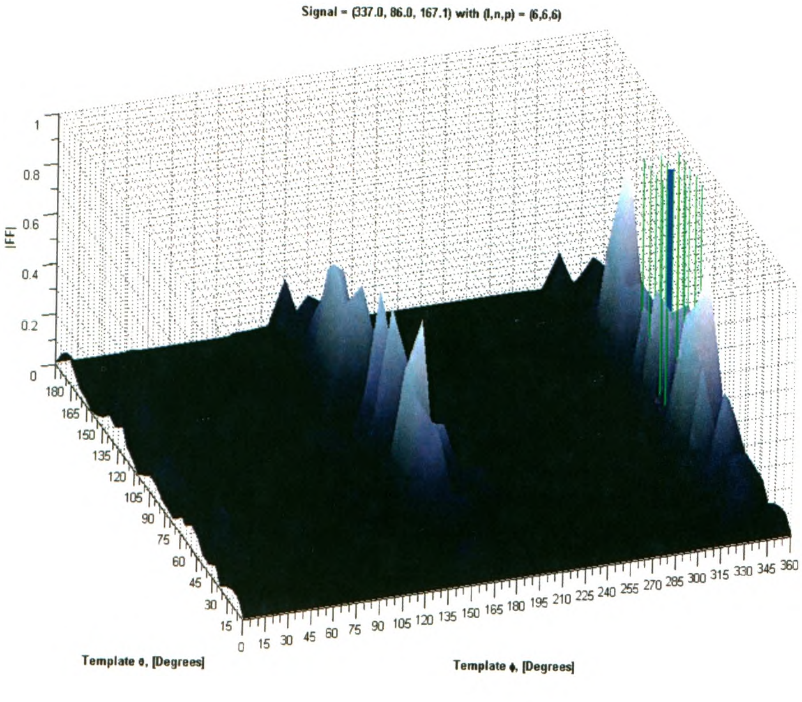

Figure 8.17: A parameter mesh used, which contained 1089 points. The thick vertical line represents the source location. The smaller vertical lines represent templates that were within a 15 degree radius of the signal.

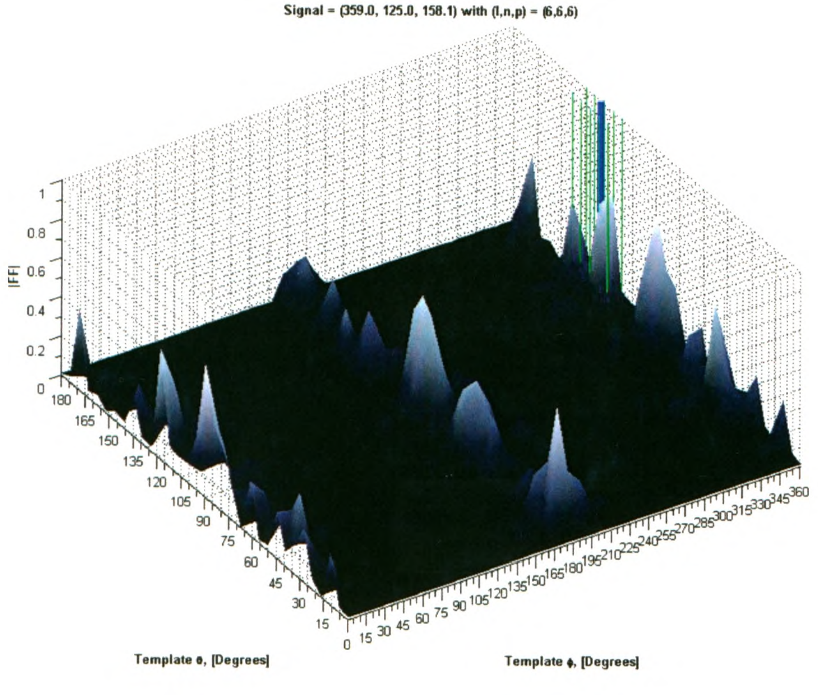

Figure 8.18: A parameter mesh used, which contained 1089 points. The thick vertical line represents the source location. The smaller vertical lines represent templates that were within a 15 degree radius of the signal.

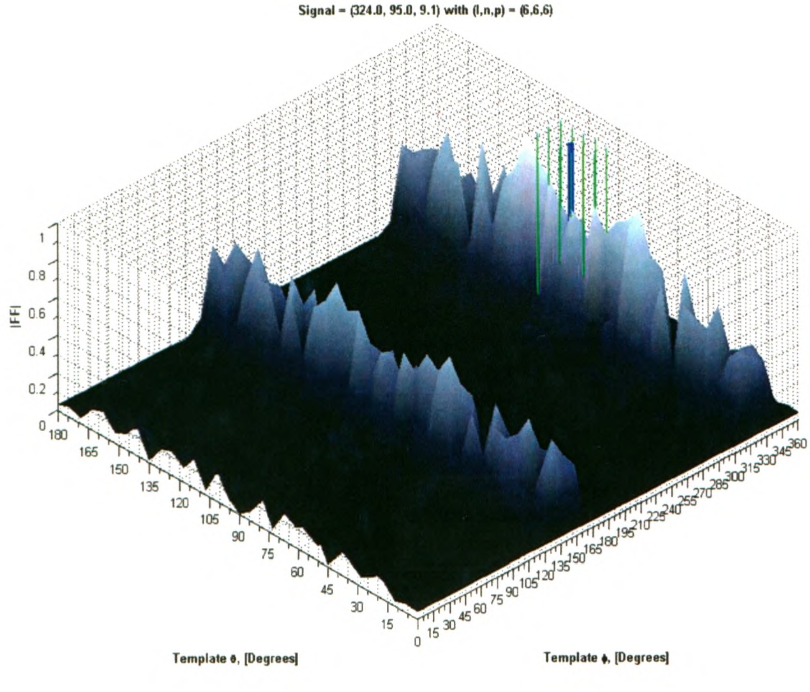

Figure 8.19: A parameter mesh used, which contained 1089 points. The thick vertical line represents the source location. The smaller vertical lines represent templates that were within a 15 degree radius of the signal.

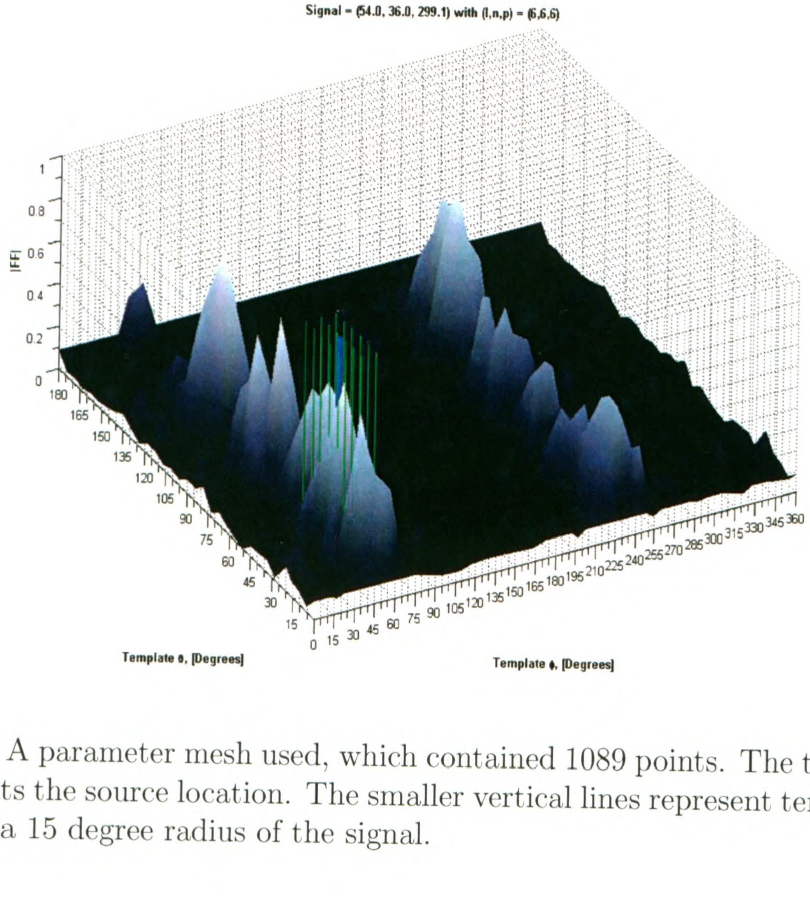

Figure 8.20: A parameter mesh used, which contained 1089 points. The thick vertical line represents the source location. The smaller vertical lines represent templates that were within a 15 degree radius of the signal.

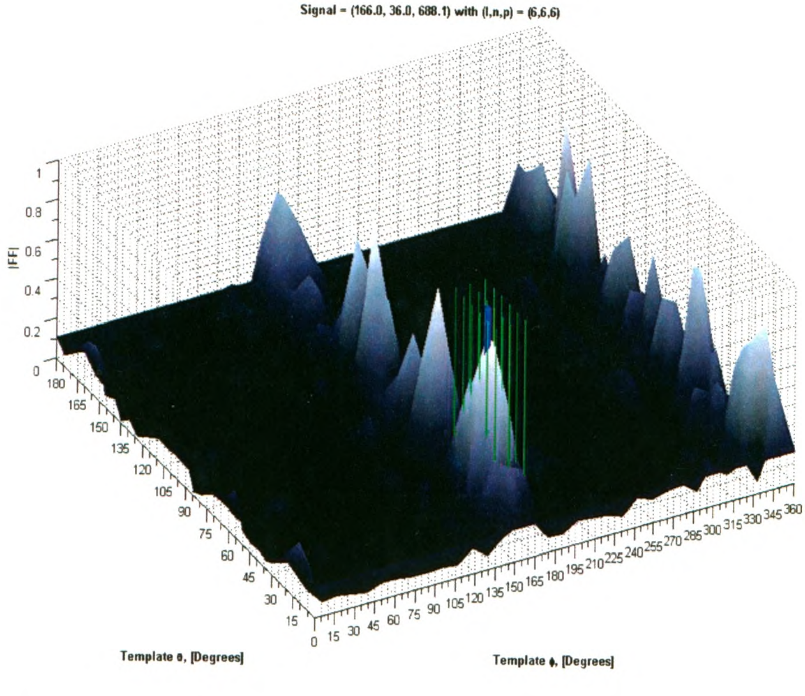

Figure 8.21: A parameter mesh used, which contained 1089 points. The thick vertical line represents the source location. The smaller vertical lines represent templates that were within a 15 degree radius of the signal.

Chapter 9

Conclusions

Matched filtering a GW pulsar signal using templates was shown to be possible. It poses a challenge for both symbolic and parallel computation. Although good values are obtained when the series summations are truncated at 10, it is desirable to use larger indices to obtain a more desirable accuracy and to do so within a reasonable runtime.

Using the Fourier transformed GW signal from a pulsar as formulated by [12] an exact analytical expression was obtained, where others used many approximations [37], for the inner product, and so fitting factor, of a simulated gravitational wave signal with a set of template functions. The expression relies on use of the special functions of mathematical physics, with the interesting connection between the signal and template being contained in the reciprocal product of two gamma functions. The gamma, Legendre, Bessel, and hypergeometric functions have importance in many applications [38]. Use of symbolic numerical method for their fast and accurate evaluation warrants further study of its own. Using a more sophisticated model signal that takes into account further effects such as perturbations due to Jupiter and the Moon also gives rise to similar gamma functions [39]. It would be interesting to explore further the connection of matched filtering to the use of templates that involve product of reciprocal Eulerian gamma functions.

The numerical studies showed that the matched filtering method gives a value significantly close to 1 for the fitting factor when the signal and template parameter sets were equal or when they were relatively close. Specifically, the statistics obtained show that if a FF has a value larger than 0.9, then there is roughly a 55-70 percent change that the signal lies within a 15 degree radius of the template giving rise to that particular FF value. This is in agreement with the results reported by Apostolatos [17].

The numerical results of Figure 8.4 show that the largest FF values are obtained along ranges of θ when $\phi_T = \phi_S$ or $\phi_T = \phi_S + 180$ degrees. The numerical aspect of this research could be advanced further by either more efficient coding of the algorithms used in the calculations, or the finding of possible symmetries in the inner products expression, which the observations hint at.

The frequency study resulted in unexpected behavior. The sharp peak that occurs only when the template frequency matches that of the signal frequency is an interesting result that warrants further study.

The improvement of the bounds presented in Equations (6.29)-(6.34) is an interesting problem to be explored. Having tighter bounds would result in a better choice for the summation indices to reach a desired accuracy for the inner products. This study is currently in progress. Development of an asymptotic expansion of the inner product using the special functions of mathematical physics would also be extremely useful. They also arise in the study of Doppler radar[1].

In an unpublished study [39], using a more sophisticated model for the GW signal from a pulsar also resulted in an analytic expression for the inner product, though much more complex – the number of summations and special functions are increased. The additional complexity is due to the Jovian, eccentric orbit, and Lunar perturbations in the Fourier transform of the GW pulsar model. Its similar inclusion of reciprocal gamma functions whose arguments involve terms from both a signal and a template, as well as results of other authors such as Buonanno et al. [40] [41], leads us to consider the possibility that the reciprocal gamma functions are playing a deeper

---

[1] private communication with Dr. S. R. Valluri and Dr. F. A. Chishtie

role than is currently known. The gamma functions have found an innumerable variety of applications, such as in problems of Quantum Mechanics, Magnetic Resonance Imaging, Meteorology, and Financial Mathematics [42, 43, 44, 45]. It is of great interest to note that the gravitational wave pulsar signal as well as the inner product of the signal and the template have the same pattern as seen in radar ambiguity signal correlations and the Wigner-Ville distribution. The latter being introduced first in the context of quantum mechanics has found important applications in the fundamental study of radar ambiguity signals. It is hardly surprising that the gamma functions envisioned by Leonhard Euler, whose Tricentennial occurred this previous year, find innumerable interesting connections and applications in ways that are not easily fathomed.

9.1 Achievements

During the progress of this thesis two papers were accepted for publication. One of them has already been published [1], and the other is due to appear in the latter part of 2008 [2]. These papers are listed in full as:

1. M. E. Normandin, A. Vajda, and S. R. Valluri, "Matched filtering a gravitational wave pulsar signal involving reciprocal gamma functions," *SNC '07: Proceedings of the 2007 international workshop on Symbolic-numeric computation*, London, Ontario, Canada., July 2007, pp. 133–141.
2. M. E. Normandin, A. Vajda, and S. R. Valluri, "Gravitational Wave Signal Templates, Pattern Recognition, and Reciprocal Eulerian Gamma Functions," *Journal of Theoretical Computer Science*, (in press).

In addition, a presentation of the results of the first paper was given in a talk at The University of Western Ontario in July 2007 at the international conference on symbolic and numerical computation. A third paper on the mathematical analysis of the spectral noise densities of GW detectors is under preparation.

9.2 Future Work

Some possible future work is the following:

1. Extension of the analytic derivation of the inner product of matched filtering to the general spectral noise density formula, Equation (4.22), would benefit multiple detectors.
2. A deeper understanding of the correlation between a GW source's azimuthal direction angle and that angle plus 180 degrees is desired because this has a great potential to be exploited as a means to speed up all-sky searches.
3. As a real-world test of the effectiveness of the thesis results, they could be applied to the simulated data of the Mock Data LISA Challenge (MLDC), and also to simulations of expected LIGO output containing signals from continuous sources such as pulsars.

Bibliography

[1] M. E. Normandin, A. Vajda, S. Valluri, Matched filtering a gravitational wave pulsar signal involving reciprocal gamma functions, in: SNC '07: Proceedings of the 2007 international workshop on Symbolic-numeric computation, ACM, New York, NY, USA, 2007, pp. 133–141. v, 92

[2] M. E. Normandin, A. Vajda, S. R. Valluri, Gravitational wave signal templates, pattern recognition, and reciprocal eulerian gamma functions, Theoretical Computer Science. v, 92

[3] H. Collins, Gravity's Shadow: The Search for Gravitational Waves, The University of Chicago Press, 2004. 1

[4] M. Bartusiak, Einstein's Unfinished Symphony, Berkley Books, New York, 2003. 1

[5] S. Hughes, S. Markla, P. Bender, C. Hogan, New physics and astronomy with the new gravitational-wave observatories, arXiv:astro-ph/0110349v2. 2, 15, 17

[6] (2008). 7

[7] J. B. Hartle, Gravity: An introduction to Einstein's General Relativity, Addison-Wesley Publishing Company, 2003. 8, 11, 12

[8] M. Maggiore, Gravitational Waves: Volume 1, Theory and Experiments, Oxford University Press, 2008. 13, 32

[9] P. Jaranowski, A. Królak, B. F. Schutz, Data analysis of gravitational-wave signals from spinning neutron stars: The signal and its detection, Phys. Rev. D 58 (6) (1998) 063001. 18, 28

[10] L. S. Collaboration, All-sky search for periodic gravitational waves in ligo s4 data, Phys. Rev. D 77 (2). 18, 19, 23, 34

[11] S. R. Valluri, J. J. Drozd, F. A. Chishtie, R. G. Biggs, M. Davison, S. V. Dhurandhar, B. S. Sathyaprakash, A study of the gravitational wave form from pulsars, Classical and Quantum Gravity 19 (2002) 1327–1334. 20, 40, 41

[12] S. R. Valluri, F. A. Chishtie, A. Vajda, The gravitational wave pulsar signal with jovian and lunar perturbations and orbital eccentricity corrections, Classical and Quantum Gravity 23 (2006) 3323–3332. 20, 90

[13] S. R. Valluri, K. M. Rao, P. Wiegert, F. A. Chishtie, A study of the gravitational wave pulsar signal with orbital and spindown effects, Canadian Journal of Physics 84 (2006) 1–7. 20

[14] L. S. Finn, Detection, measurement, and gravitational radiation, Phys. Rev. D 46 (12) (1992) 5236–5249. 20, 21

[15] L. A. Wainstein, V. D. Zubakov, Extraction of signals from noise, Prentice-Hall, Inc, 1962. 20

[16] J. Aldrich, R. a. fisher and the making of maximum likelihood 1912-1922, Statistical Science 12 (3). 25

[17] T. A. Apostolatos, Search templates for gravitational waves from precessing, inspiraling binaries, Phys. Rev. D 52 (2) (1995) 605–620. 27, 29, 30, 91

[18] C. Cutler, E. E. Flanagan, Gravitational waves from merging compact binaries: How accurately can one extract the binary's parameters from the inspiral waveform?, Phys. Rev. D 49 (6) (1994) 2658–2697. 27, 29

[19] R. Balasubramanian, S. V. Dhurandhar, Performance of newtonian filters in detecting gravitational waves from coalescing binaries, Phys. Rev. D 50 (10) (1994) 6080–6088. 29

[20] R. Prix, Template-based searches for gravitational waves: efficient lattice covering of flat parameter spaces, arXiv:0707.0428v1 [gr-qc]. 33, 35

[21] R. Balasubramanian, B. S. Sathyaprakash, S. V. Dhurandhar, Gravitational waves from coalescing binaries: Detection strategies and monte carlo estimation of parameters, Phys. Rev. D 53 (6) (1996) 3033–3055. 35

[22] B. J. Owen, Search templates for gravitational waves from inspiraling binaries: Choice of template spacing, Phys. Rev. D 53 (12) (1996) 6749–6761. 35

[23] R. A. Finkel, J. L. Bentley, Quad trees a data structure for retrieval on composite keys, Acta Informatica 4 (1). 37

[24] I. Gholami, C. Cutler, B. Krishnan, Optimized search strategies for continuous gravitational waves, Gravitational Wave Data Analysis Workshop 9. 37, 38

[25] B. H. Bransden, C. J. Joachain, Quantum Mechanics, Second Edition, Prentice Hall, 2000. 41

[26] A. P. Prudnikov, Y. A. Brychkov, O. I. Marichev, Integrals and Series, Volume 2: Special Functions, Vol. 2, Gordon and Breach Science Publishers S.A, 1986. 49, 50

[27] G. Lohoefer, Inequalities for the associated legendre functions, Journal of Approximation Theory 95 (1998) 178–193. 54

[28] N. M. Temme, Special Functions: An Introduction to the Classical Functions of Mathematical Physics, Wiley Interscience, 1996. 54

[29] B. Stroustrup, The C++ Programming Language, 3rd Edition, Addison-Wesley Publishing Company, 2000. 56

[30] M. Inc., Matlab (2008). 56

[31] www.sharcnet.ca, Shared hierarchial academic research computing network (sharcnet) (2008). 56, 58

[32] GNU, Gnu scientific library (2008). 57

[33] GNU, Gnu general public license (2008). 57

[34] GNU, Gnu multiple precision arithmetic library (2008). 62

[35] W. Kahan, Further remarks on reducing truncation errors, Communications of the ACM 8 (1). 62

[36] Wikipedia, Kahan summation algorithm (Jul 2008). 62

[37] D. C. Srivastava, S. K. Sahay, Data analysis of continuous gravitational wave: all-sky search and study of templates, Monthly Notices of the Royal Astronomical Society 337 (1) (2002) 322–326. 90

[38] V. Adamchik, On the barnes function., in: ISSAC, 2001, pp. 15–20. 90

[39] M. E. Normandin, S. R. Valluri (2008). 90, 91

[40] A. Buonanno, Y. Chen, M. Vallisneri, Detection template families for gravitational waves from the final stages of binaryˇblack-hole inspirals: Nonspinning case, Phys. Rev. D 67 (2) (2003) 024016. 91

[41] A. Buonanno, Y. Chen, M. Vallisneri, Detecting gravitational waves from precessing binaries of spinning compact objects: Adiabatic limit, Phys. Rev. D 67 (2003) 104025.
URL `http://www.citebase.org/abstract?id=oai:arXiv.org:gr-qc/02110`
91

[42] C. F. Starmer, D. O. Clark, Computer computations of cardiac output using the gamma function, Journal of Applied Physiology 28 (2) (1970) 219–220. 92

[43] H. C. S. Thom, A note on the gamma distribution, Monthly Weather Review 86 (4) (1958) 117122. 92

[44] V. S. Adamchik, The multiple gamma function and its application to computation of series, The Ramanujan Journal 9 (2005) 271–288. 92

[45] J. M. Ollinger, M. Corbetta, G. L. Shulman, Separating processes within a trial in event-related functional mri, NeuroImage 13 (1) (2001) 218–229. 92